Acta Materialia 262 (2024) 119415

Contents lists available at ScienceDirect

Acta Materialia

journal homepage: www.elsevier.com/locate/actamat

Full length article

Local lattice distortions and the structural instabilities in bcc Nb–Ta–Ti–Hf high-entropy alloys: An *ab initio* computational study

Pedro P.P.O. Borges *, Robert O. Ritchie, Mark Asta **

Materials Sciences Division, Lawrence Berkeley National Laboratory, Berkeley, CA 94720, USA
Department of Materials Science and Engineering, University of California, Berkeley, CA 94720, USA

ARTICLE INFO

Keywords:
High-entropy alloys
Body-centered cubic metals
Density functional theory
Lattice distortions
Structural phase stability

ABSTRACT

Local lattice distortions (LLD) and structural stability of body-centered cubic (bcc) Nb–Ta–Ti–Hf high-entropy alloys (HEAs) are studied as functions of composition employing *ab initio* density-functional theory calculations, with specific focus on the role of the relative concentrations of group IV (Ti and Hf) *versus* group V (Nb and Ta) elements. Calculated results are presented as a function of composition x in $Nb_xTa_{0.25}Ti_{(0.75-x)/2}Hf_{(0.75-x)/2}$ alloys, for elastic moduli, phonon spectral functions, LLD and structural energy differences for the bcc and competing hexagonal close-packed (hcp) and ω phases. The results highlight the important role of group V elements and LLD in stabilizing the bcc structure. They further reveal how composition x can be tuned to alter both the magnitude of the LLD and structural energy differences. Specifically, the magnitude of the structural energy differences, and elastic and dynamic stability of the bcc phase, are enhanced with increasing x, while the LLD increase in magnitude as this concentration is decreased. The results also show evidence of correlated LLD at lower values of x, reflecting local structural distortions towards the ω phase, but not hcp. The degree of ω-collapse is nevertheless partial *i.e.*, transformation towards this phase is not observed to be complete due to the presence of Ta and Nb. At lower values of x we further find an energy landscape characterized by multiple, nearly degenerate local energy minima for different values of the LLD.

1. Introduction

Body-centered cubic (bcc) high entropy alloys (HEAs) formed as mixtures of group IV (Ti, Zr, Hf), V (V, Nb, Ta) and VI (Cr, Mo, W) elements have been demonstrated to form as single-phase solid solutions over a wide compositional range [1–3]. These HEAs have received great interest due to their unique combinations of materials properties, spanning excellent high-temperature strength [4–6] and high low temperature ductility [7–9], depending on composition. Theoretical and experimental research probing the origins of these properties have highlighted the important role of local lattice distortions (LLD) arising from atomic-size [10,11] and elastic [12,13] misfit, as well as twinning [7] and transformation-induced plasticity (TRIP) [7,14,15] arising from competing stability of metastable phases with the bcc structure. The TRIP mechanism has been shown to be particularly relevant in bcc HEAs enriched in group IV elements, particularly for compositions that demonstrate high ductility at low temperatures [7–9].

The understanding of LLD, twinning and phase competition in bcc HEAs, and how they are affected by composition, has been advanced through computational studies based on density-functional theory (DFT). Focusing specifically on bcc HEAs with high concentrations of group IV elements, these calculations have quantified the energetic phase competition between bcc, face-centered cubic (fcc), hexagonal close-packed (hcp) and ω structures, and how they are impacted by the ratio of the concentrations of group IV to group V elements [16,17], as well as the important role of LLD [17]. The effects of composition on elastic [16,18] and dynamic (as characterized by the phonons) stability [19,20] of the bcc lattice has been reported, with the role of LLD highlighted in the latter case. Some of these studies [17,18] have also highlighted how high concentrations of group IV elements lead to signatures of local structural distortions of the bcc lattice towards competing phases.

The current work builds on these previous computational studies, employing DFT calculations to thoroughly characterize the interrelation between composition, phase competition, elastic and dynamic stability, and LLD, in the Nb–Ta–Ti–Hf system. Interest in this system is motivated in part by the experimental reports of high ductility and strength in related alloys [5,7,21], particularly at room temperature and low temperatures. From a more fundamental perspective, this system provides a platform to understand the impact of group IV to

* Corresponding author at: Department of Materials Science and Engineering, University of California, Berkeley, CA 94720, USA
** Corresponding author.
E-mail addresses: pedro_borges@berkeley.edu (P.P.P.O. Borges), mdasta@berkeley.edu (M. Asta).

https://doi.org/10.1016/j.actamat.2023.119415
Received 27 June 2023; Received in revised form 8 September 2023; Accepted 6 October 2023
Available online 10 October 2023

group V composition on the intrinsic structural and energetic properties underlying phase and lattice stability. Specifically, we present detailed analyses of calculated elastic moduli, phonon spectral functions, LLD, and structural energy differences between bcc, hcp and ω phases, over a wide range of compositions in $Nb_xTa_{0.25}Ti_{(0.75-x)/2}Hf_{(0.75-x)/2}$, with x ranging from 0 to 0.5. The results demonstrate the effects of composition and LLD in governing the energetic, elastic and dynamic stability of the bcc structure. It also highlights how the incipient stability of the ω phase is manifested in the LLD and how a surprisingly complex energy landscape characterized by multiple, nearly degenerate structures can arise from the competition between structural preferences dictated by the group IV and V elements. The results provide potentially important guidelines for designing metastability in bcc HEAs, and demonstrate phenomena that could have important implications for deformation processes.

2. Methods

2.1. Ab initio calculations

First principles calculations are performed using density functional theory (DFT) implemented in the Vienna *ab initio* simulation package (VASP) code [22–24]. We employ the projected-augmented-wave (PAW) method [25,26] in combination with the Perdew–Burke–Ernzerhof generalized gradient approximation for the exchange–correlation potential [27]. Wavefunctions are expanded in a plane-wave basis set with a kinetic energy cutoff of 400 eV. The PAW potentials employed in the calculations treat as valence 11, 5, 4 and 4 electrons for Nb, Ta, Ti, and Hf, respectively. This choice excludes consideration of the semi-core p-states as valence for Ti and Hf; we have verified that this approximation does not affect the stability of the bcc structure, as detailed in the supplementary materials. We employ the Methfessel–Paxton scheme [28] with a smearing of 0.2 eV to broaden the electronic occupation. Atomic positions are relaxed using the conjugate gradient algorithm until residual ionic forces have magnitudes below 10^{-3} eV/Å.

Phonon frequencies are calculated at the harmonic level employing the framework of finite differences, using the Phonopy package [29]. In order to enhance precision, we use an energy converge criterion of $<10^{-7}$ eV for the electron self-consistency criterion in these calculations. Calculations of phonon spectral functions from zone-unfolding of the phonon spectra are performed using the method and publicly available code from Ref. [30].

Finite temperature simulations are performed with *ab initio* molecular dynamics (AIMD) to explore potential energy landscapes. In these simulations, the same methods and convergence parameters as described above are employed. Simulations are performed in the NVT-ensemble, using the equilibrium lattice parameter calculated at absolute zero and the Langevin thermostat [31] with a friction coefficient of $10\,ps^{-1}$. Simulations are carried-out using a time step of 2 fs.

2.2. Simulation cells

We study eleven compositions of $Nb_xTa_{0.25}Ti_{(0.75-x)/2}Hf_{(0.75-x)/2}$ HEAs with x ranging from 0 to 0.5, where chemical disorder is mimicked using the special quasirandom structures (SQS) approach [32]. The SQS are generated using the MCSQS [33] package in the Alloy Theoretic Automated Toolkit (ATAT), and are constructed to provide correlation functions for the first two neighbor shells that approximate a random solution for all constituent elements. All simulation cells contain 54 atoms, corresponding to a $3 \times 3 \times 3$ expansion of the conventional bcc and hcp cells and to a $3 \times 3 \times 2$ expansion of the conventional ω cell. Since number of atoms (54) in the SQS cells is not commensurate with some of the nominal compositions listed above, we list the exact number of each atom type for each values of x in the supplementary materials.

To sample the Brillouin zone in the DFT calculations, we make use of a Γ-centered $6 \times 6 \times 6$ k-point grid in the case of the bcc SQS supercell and a $6 \times 6 \times 4$ k-point grid in the case of the hcp and ω SQS supercells. All DFT calculations are performed at constant cell shape and volume.

The lattice parameter of the ideal bcc structure (a_{bcc}) is chosen to be the reference to build the hcp and ω structures *via* the known transformation paths relating these structures to the bcc lattice. Specifically, considering the Burgers [34] relation for the hcp and bcc phases, the ideal lattice parameter of the hcp structure (a_{hcp}) can be obtained using $a_{hcp} \approx 0.89\, a_{bcc}$, assuming the tetragonal path as discussed in Section 3.2 [35]. We also assume an ideal hexagonal angle of 120°, corresponding to a c/a ratio of ≈1.63, which was shown to be a minimum along the transformation path in pure bcc Ti and Hf [36]. The ideal ω phase can be obtained by a complete collapse of alternate pairs of $\{111\}_{bcc}$ planes [37,38]. The resulting two-layered structure has a hexagonal lattice with P6/mmm space group in the absence of compositional disorder. The relation between the lattice parameter of bcc and ω phases is given by: $a_\omega = \sqrt{2}\, a_{bcc}$ and $c_\omega = \sqrt{3}/2\, a_{bcc}$. In all of the supercell calculations we keep the supercell shape constrained to cubic for bcc and to the geometry described above for hcp and ω.

2.3. Elastic constants

Elastic moduli (C_{ij}) are obtained from stress–strain relations using linear elasticity theory [39,40]. We consider ten sets of deformation: uniaxial strain along X, Y and Z; simple shear along XY, XZ and YZ; in-plane strain, shear along (111) and two sets of mixed strains. We apply Voigt convention and strain amplitudes are equal to ±0.01 and ±0.02 Å/Å. For every deformed configuration, atomic positions are optimized and the stress tensor is calculated on the basis of the DFT formalism. C_{ij} are then computed *via* a least-squares fit over all strain conditions, assuming cubic (bcc phase) or hexagonal (hcp and ω phases) symmetry.

3. Results and discussion

This section presents calculated results concerning the effects of group IV element concentration on the lattice stability and structural distortions of Nb–Ta–Ti–Hf HEAs, highlighting properties that are relevant to mechanical behavior and structural transformation. The presentation begins with a discussion of the properties of the reference ideal bcc structures derived from the equation of state, including trends in lattice parameters, cohesive energies and bulk moduli (Section 3.1). The mechanical stability of the bcc lattice relative to homogeneous elastic distortions is then analyzed through results for elastic moduli, and energy *versus* strain relations along pathways associated with transformations of the bcc lattice to fcc and hcp structures (Section 3.2). These results are complemented by an analysis of dynamical structural stability with respect to finite-wavelength phonons, including those associated with transformation to ω, and the shuffle components of the transformation to hcp (Section 3.3). Section 3.4 provides additional information related to structural stability, focusing specifically on the structural energy differences between bcc, hcp and ω phases. Finally, Section 3.5 is devoted to the important topic of local lattice distortions (LLD). We present results showing the effects of group IV element concentration on the magnitude of the LLD (Section 3.5.1), and the relation of the LLD to charge-transfer. The nature of the LLD in the bcc phase is then analyzed (Section 3.5.2) in terms of local structural descriptors related to transformations to the hcp and ω phases, highlighting the important features of the potential energy landscape (Section 3.5.3), and also the mechanisms underlying substantial ω-like distortions at high group IV concentrations (Section 3.5.4).

Table 1
Ideal bcc structure. Average atomic mass ($\bar{m}$), bcc cohesive energy (E^{bcc}_{ideal}), equilibrium lattice parameter (a_{bcc}) and bulk modulus (B) obtained by fitting the Birch–Murnaghan equation of state to energy–volume relations obtained for pure Nb, Ta, Ti, Hf, the binary $Ti_{0.5}Hf_{0.5}$ and $Nb_xTa_{0.25}Ti_{(0.75-x)/2}Hf_{(0.75-x)/2}$ systems with atoms constrained to reside on ideal bcc lattice sites.

Composition[a]	$\bar{m}$ (u/atom)	E^{bcc}_{ideal} (eV/atom)	a_{bcc} (Å)	B (GPa)
pure Nb	92.91	−10.90	3.324	170
pure Ta	180.95	−11.86	3.308	202
pure Ti	47.87	−7.66	3.237	112
pure Hf	178.49	−9.78	3.532	107
$Ti_{0.5}Hf_{0.5}$	113.18	−8.67	3.397	105
0	130.12	−9.47	3.365	126
5	129.11	−9.49	3.361	128
10	128.09	−9.63	3.355	134
15	127.08	−9.69	3.351	136
20	126.07	−9.71	3.350	138
25	125.05	−9.85	3.344	144
30	124.04	−9.90	3.342	148
35	123.03	−9.92	3.339	150
40	122.01	−10.06	3.335	156
45	121.00	−10.12	3.334	158
50	119.98	−10.14	3.332	161

[a] The bottom eleven rows give x in at.%.

3.1. Properties of reference ideal bcc structures

We first focus on the ground state properties of the ideal bcc structure *i.e.*, considering atoms confined to ideal bcc lattice sites at zero temperature. The ideal bcc structure is used as reference to build the hcp and ω structures in the discussion of energetic relative stability (see Section 3.4). In addition, although the state is idealized, it allows to obtain preliminary insights on the effects of the relative concentrations of group V (namely Nb) and group IV (Ti and Hf). Table 1 presents calculated results for the cohesive energies and lattice parameters for these idealized bcc HEAs and their pure constituents.

Additionally, for reference, in the discussion of calculated phonons below (see Section 3.3) an analysis of mass effects becomes relevant. As listed in Table 1, if we take the atomic mass of Nb as reference, the atomic masses of Ti and Hf are 48% and 92% lighter and heavier, respectively. As such, these two effects counteract, resulting in a small net decrease of the HEA average mass ($\bar{m}$) such that $\bar{m}$ decreases as the Nb concentration increases, showing a variation of −8.5% across our studied compositions.

Using a fit of the energy–volume relation over the third-order Birch–Murnaghan equation of state (EOS) [39], we obtain the equilibrium bcc energy (E^{bcc}_{ideal}), lattice parameter (a_{bcc}) and bulk modulus (B) listed in Table 1. Results show a monotonic decrease of the bcc energy, indicating an enhancement of the bcc structural stability with respect to the constituent atoms with increasing Nb concentration. The lattice parameter slightly decreases with increasing x, consistent with the smaller size of Nb compared to Hf, showing a total volume variation of −0.55 Å^3/atom from $x = 0$ to 50 at.%. The decrease of interatomic spacing is correlated with an increase of bond strength, as reflected by a stiffening of the bulk modulus. Since the bulk modulus of pure Nb is greater than Ti and Hf, this stiffening is also expected due to the increase of its concentration. We highlight that for each composition we use four different SQS models to perform the EOS analysis, and the differences between the obtained values of the lattice parameter are smaller than 0.005 Å across these models. We therefore adopted the same lattice parameter (as presented in Table 1) across all SQS configurations at a given composition throughout this work.

In order to distinguish the interplay of Ta concentration from Nb, we compare the results obtained for the binary bcc $Ti_{0.5}Hf_{0.5}$ and $Ta_{0.25}Ti_{0.375}Hf_{0.375}$ (*i.e.*, $Nb_xTa_{0.25}Ti_{(0.75-x)/2}Hf_{(0.75-x)/2}$ with x = 0 at.%). Table 1 shows that the addition of Ta to the binary $Ti_{0.5}Hf_{0.5}$ alloy provides pronounced stiffening of the bulk modulus (+20%) and leads to a larger magnitude for the bcc energy, both indicating that Ta significantly enhances the bcc structural stability.

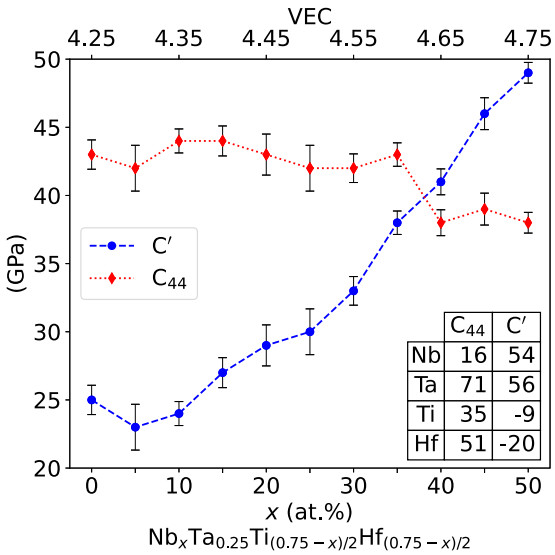

Fig. 1. Elastic stability of the bcc phase. Calculated values of the tetragonal shear modulus (C', blue circles) and C_{44} (red diamonds) for bcc $Nb_xTa_{0.25}Ti_{(0.75-x)/2}Hf_{(0.75-x)/2}$ are plotted *versus* Nb concentration (lower x-axis) and valence electron count (VEC, upper x-axis). Reference values of C' and C_{44} for the pure constituent elements in the bcc structure are provided in the inset. In the case of HEAs, values are averaged over four different SQS models, with the error bars indicating minimum and maximum calculated values. (For interpretation of the references to color in this figure legend, the reader is referred to the web version of this article.)

3.2. Elastic moduli and elastic stability

We consider next the elastic stability of the compositions considered in this work. For a cubic crystal, the criteria for elastic stability can be formulated as B, C_{44} and $C' > 0$ [41], where $C' = (C_{11} - C_{12})/2$ is the tetragonal shear modulus. The single-crystal elastic moduli C_{ij} are computed from calculated stress–strain relations as described in the Methods section. Atomic configurations used to compute C_{ij} include local lattice distortions (LLD) *i.e.*, atomic positions are fully relaxed before applying the finite strains unless otherwise noted.

We first discuss the elastic stability of pure bcc Nb, Ta, Ti and Hf. Fig. 1 (inset) shows that while Nb and Ta are elastically stable, both Ti and Hf show $C' < 0$ reflecting an unstable bcc lattice. This instability is documented in the literature and is associated with the bcc→hcp transformation [36,42]. We also note the low value of C_{44} in Nb relative to experimental measurements, which is a trend consistent with prior DFT results [43–45]; while calculated values are consistently lower than experiments, they show a range of values due to sensitivities to the nature of the pseudopotential or PAW approximations and their numerical implementations.

Fig. 1 plots for bcc $Nb_xTa_{0.25}Ti_{(0.75-x)/2}Hf_{(0.75-x)/2}$ the calculated values *versus* x of C_{44} and C' averaged over four different SQS models. In order to ensure the relevance of our results, we compare the obtained bulk modulus using the EOS and the one calculated from elastic constants. We verify that results provided by these two different methods are in excellent agreement, showing a maximum relative difference smaller than 5% (see supplementary materials). Furthermore, we note that computed values for C_{ij} by DFT calculations agree to within 10% with experimentally measured results for bcc NbTiZrHf reported in Refs. [46,47].

As indicated by the calculated results in Fig. 1, all bcc $Nb_xTa_{0.25}Ti_{(0.75-x)/2}Hf_{(0.75-x)/2}$ systems are elastically stable even at low Nb concentrations. The calculated C_{ij} values are averaged over four SQS models, each displaying different degrees of LLD in the relaxed configurations, as described below. We observe that relative differences between the average and extremum C_{ij} values across these

Table 2
The role of Ta concentration and local lattice distortions (LLD) on the elastic stability of bcc, ω and hcp structures. Elastic moduli (C_{ij}, in GPa) with and without LLD are obtained *via* the finite distortions approach for $Ti_{0.5}Hf_{0.5}$ and $Ta_{0.25}Ti_{0.375}Hf_{0.375}$. The bulk modulus ($B$, in GPa) and tetragonal shear modulus (C', in GPa) are calculated using the obtained C_{ij}.

	Phase	LLD	C_{11}	C_{12}	C_{13}	C_{33}	C_{44}	B	C'
$Ti_{0.5}Hf_{0.5}$	bcc	w/o	88	115	–	–	47	106	−13
	ω	w/o	194	81	53	243	53	111	56
	hcp	w/o	198	72	88	201	56	121	63
$Ta_{0.25}Ti_{0.375}Hf_{0.375}$	bcc	w/o	140	119	–	–	41	126	10
	bcc	w/	166	109	–	–	48	128	28
	ω	w/o	217	113	72	246	44	133	52
	ω	w/	204	108	84	230	43	132	48
	hcp	w/o	219	113	113	247	32	151	53
	hcp	w/	229	104	108	235	41	148	62

SQS structures are less than 5% across all compositions. We therefore conclude that the obtained elastic properties are not strongly affected by the difference in chemical distribution across the different SQS, and further that the variations in the magnitudes of LLD do not significantly influence the magnitude of the elastic constants.

Fig. 1 shows that C_{44} is almost constant up to intermediate Nb concentrations and then softens when x becomes greater than 40 at.%, which correlates with the high Nb concentration and the low value of C_{44} for this element as previously discussed. In contrast, we evidence a pronounced stiffening of the tetragonal shear modulus as the Nb concentration increases, with C' at $x = 50$ at.% being almost twice that for $x = 0$ at.%. We however observe a softening of C' from $x = 0$ to 5 at.%, which arises from the greater relative increase of C_{12} compared to C_{11} (see supplementary materials).

The tetragonal shear modulus connects the bcc to the hcp and fcc structures *via* the Burgers [34] and Bain [48] paths, respectively. Using the bcc structure as reference, both paths can be described by a single continuous strain order parameter $\boldsymbol{\eta}_{\text{tetra}} = (-\delta/2, -\delta/2, \delta, 0, 0, 0)$, where $\boldsymbol{\eta}_{\text{tetra}}$ indicates the Lagrangian tetragonal strain tensor in Voigt notation and δ is the strain amplitude. The resulting body-centered tetragonal lattice has c/a ratios of $\sqrt[4]{3/2}$ and $\sqrt{2}$ in the case of the hcp and fcc structures respectively, corresponding to a strain amplitude of $\delta \approx -0.10$ and $\delta \approx 0.23$, respectively. Since the change in energy (ΔE) along this path is given by $\Delta E \propto C' \delta^2$ around the bcc configuration, a small value of the tetragonal shear modulus implies a low energy barrier for structural change.

A more rigorous approach to study the bcc→hcp transformation would consider an orthorhombic shear deformation as formulated by Ref. [49]. In this work, we consider a first order approximation of the strain for this transformation [35], coinciding with the tetragonal case as discussed above, which was shown to be accurate enough to model the Burgers path energy landscape in pure group IV metals [50], group IV–V binaries [35] and even group IV enriched bcc HEAs [20]. In order to complete the bcc→hcp transformation, an alternating shuffle displacement of $\{110\}_{\text{bcc}}$ planes is required. Here we focus only on the shear part of the Burgers path and the shuffle is discussed in Section 3.5.

Fig. 2 shows the calculated strain–energy profiles along the Bain and Burgers tetragonal paths for three different Nb concentrations ($x = 0$, 25 and 50 at.%). The effect of LLD is incorporated through ionic relaxations at each value of δ. We evidence that the bcc phase is a minimum with respect to the strains corresponding to the hcp and fcc structures. Around the minimum, the stiffening of the energy curvature around $\delta = 0$ (*i.e.*, the bcc structure) with increasing Nb concentration reflects the increasing magnitude of the tetragonal shear modulus, consistent with the results in Fig. 1. The fcc configuration is however a local maximum along the Bain path and is thus elastically unstable, with the instability being enhanced as the Nb concentration increases. Relaxed configurations can only be obtained thanks to the high symmetry of the fcc network and do not correspond to a stable lattice arrangement of the Nb–Ta–Ti–Hf systems considered.

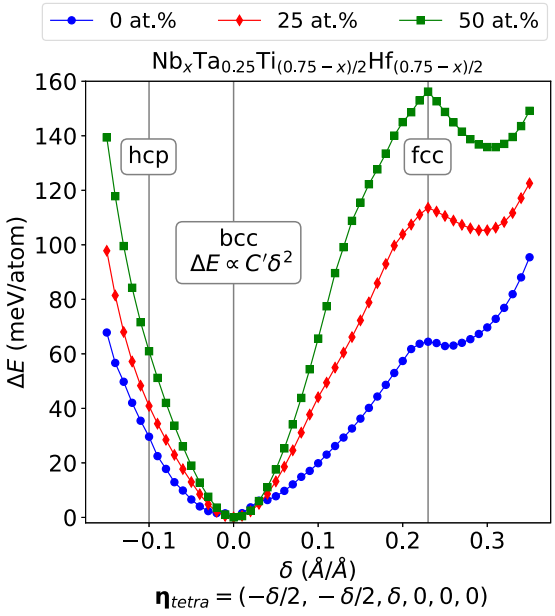

Fig. 2. Burgers and Bain tetragonal paths connecting the bcc to the hcp and fcc phases, respectively. Nb concentration (x) in $Nb_xTa_{0.25}Ti_{(0.75-x)/2}Hf_{(0.75-x)/2}$ systems is equal to 0 at.% (blue circles), 25 at.% (red diamonds) and 50 at.% (green squares). Ionic relaxation is performed for each strain amplitude (δ) in calculations of the corresponding elastic energy (ΔE). (For interpretation of the references to color in this figure legend, the reader is referred to the web version of this article.)

For the tetragonal compressive strain corresponding to the hcp structure (see Fig. 2), the energy is not a local extremum (minimum or maximum). With further increase of the strain amplitude (in absolute value), the elastic energy rapidly increases, to a degree that is enhanced with increasing Nb concentration. Overall, the Burgers and Bain tetragonal paths of our studied bcc HEAs behave similarly to pure group V elements, and are qualitatively distinct from pure group IV elements. Specifically, Ref. [50] calculates the energy *versus* tetragonal strain for pure bcc elements, showing that the group IV metals display a local maximum around the bcc configuration along the Burgers and Bain paths, in contrast to the results for the HEAs presented in Fig. 2, but qualitatively similar to the results for group V elements.

The results in this sub-section establish the elastic stability of the bcc structure for $Nb_xTa_{0.25}Ti_{(0.75-x)/2}Hf_{(0.75-x)/2}$ systems, even for the case where $x = 0$ at.% *i.e.*, the $Ta_{0.25}Ti_{0.375}Hf_{0.375}$. We now investigate the role of lattice distortions and Ta concentration on the elastic stabilization. As such, we first study the elastic properties of the binary $Ti_{0.5}Hf_{0.5}$. We find that, upon ionic forces relaxation, the bcc $Ti_{0.5}Hf_{0.5}$ structure spontaneously undergoes a structural transformation towards the ω phase. We identify the structural reconstruction based on the descriptor proposed in Section 3.5.2 (which takes a value of $p_1 - p_2 \cong 0.90$ in the relaxed structure), complemented by a coordination analysis of pair separation distance and analysis of the LLD in the relaxed structure (which takes a value of ~0.040 Å relative to the ideal ω structure). In that case, it is only possible to obtain elastic constants of the bcc structure for this composition by constraining the atoms to reside on ideal lattice sites. Table 2 shows the calculated C_{ij} using the finite distortions approach with atoms constrained to (scaled) bcc lattice sites. The obtained C' of the bcc $Ti_{0.5}Hf_{0.5}$ is negative, indicating elastic instability. In contrast, both hcp and ω phases are elastically stable. We highlight that the obtained C_{ij} for all three phases (bcc, hcp and ω) calculated here for $Ti_{0.5}Hf_{0.5}$ agree well with previous calculations [51,52], to within 5%.

Table 2 shows the obtained elastic properties of the $Ta_{0.25}Ti_{0.375}Hf_{0.375}$ with and without LLD. In the case of the bcc structure, results show that while LLD provide noticeable increase of the tetragonal

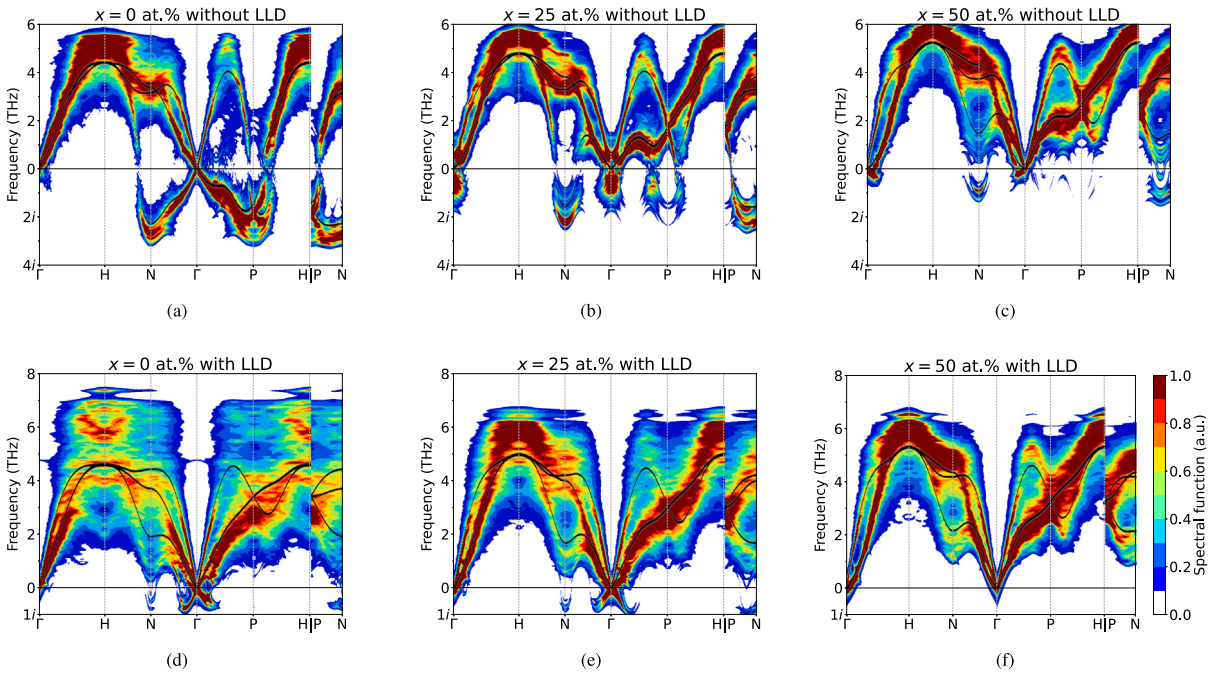

Fig. 3. Calculated phonon spectral functions for bcc $Nb_xTa_{0.25}Ti_{(0.75-x)/2}Hf_{(0.75-x)/2}$ systems. Panels (a)–(c) plot results for atoms constrained to reside on ideal bcc lattice sites and (d)–(f) accounting for local lattice distortions (LLD) resulting from the relaxation of these positions. Nb content (x) is equal to 0 at.% in (a) and (d), 25 at.% in (b) and (e), and 50 at.% in (c) and (f). The color map indicates phonon spectral functions including both mass and forces fluctuations, while black solid lines show results obtained using the virtual-crystal approximation. (For interpretation of the references to color in this figure legend, the reader is referred to the web version of this article.)

shear modulus, and thus enhance the stability of the bcc lattice, they are not the sole mechanism of the elastic stabilization. Composition effects associated with adding 25 at.% Ta to the binary $Ti_{0.5}Hf_{0.5}$ result in a positive C' even considering atoms constrained to ideal lattice sites. The results thus highlight that there is a critical Ta concentration required to elastically stabilize the bcc structure, as reported previously in calculations for related group IV enriched bcc HEAs [18].

Interestingly, Table 2 shows that ω and hcp $Ta_{0.25}Ti_{0.375}Hf_{0.375}$ are also elastically stable with or without LLD. On top of that, the inclusion of LLD does not provide significant changes on the hexagonal elastic constants. The main effect of LLD is on the hexagonal symmetry condition related to volume conservation defined as: $(C_{11} + C_{12} + 2C_{33} - 4C_{13})/6 > 0$ [53]. In the case of the ω phase, this quantity is approximately equal to 89 and 73 GPa respectively without and with LLD, corresponding to a softening of more than 20% as a result of the symmetry breaking of basal planes produced by LLD.

3.3. Phonons and dynamical instabilities

We consider next the dynamical stability of the bcc structure, reflected by the phonon frequencies $\nu(\mathbf{k})$, where $\mathbf{k}$ is the wave-vector [54]. Notably, phonon softening at zero temperature in pure bcc group IV metals along the 1/2[110] and 2/3[111] directions are associated with a structural transformation towards the hcp and ω phases, respectively [36,42,55].

At the harmonic level, we employ the finite differences approach to obtain the phonon frequencies [29]. All phonon calculations are performed on a 54-atoms cell and band unfolding is carried out using phonon modes decomposition [30] according to the translational symmetry of the primitive bcc cell. Phonon dispersion relations for a disordered materials are most generally described by a spectral function which provides the "weight" associated with each frequency of the phonon spectrum [30], and which are the proper representation of the phonons in a disordered alloy [19]; conclusions concerning dynamical stability are made based upon these results in what follows. Rather than the sharp peaks associated with elemental crystals, these spectral functions are broadened by the compositional disorder observed in HEAs [19].

Fig. 3 shows the computed phonon spectra considering two scenarios: one (without LLD) with the reference atom positions for the phonon calculations associated with ideal lattice sites, and the other (with LLD) accounting for local lattice displacements resulting from relaxation of these atomic positions. Results are again presented for bcc $Nb_xTa_{0.25}Ti_{(0.75-x)/2}Hf_{(0.75-x)/2}$ HEAs for x equal to 0, 25 and 50 at.%. The colored features in Fig. 3 represent the spectral weight of the calculated phonons. Before discussing these results, we first consider the phonon frequencies provided by the solid lines, which were obtained for an idealized bcc crystal modeled by the virtual crystal approximation (VCA), to later highlight the effects of mass and force-constant disorder (absent in the VCA) on the calculated spectral functions.

In the VCA framework, phonon frequencies are calculated using the system average atomic mass and force constants are averaged according to the bcc crystal symmetries [30]. Although the VCA does not reproduce the full complexity of the spectral functions (as noted in Ref. [19]), it does highlight some important trends that are discussed in more detail in the context of the spectral functions below. First, for $x = 0$ and 25 at.%, the VCA phonon dispersion curves show ranges of $\mathbf{k}$ with imaginary frequencies, indicating dynamic instability, in the systems with atoms on ideal lattice positions (see Figs. 3(a) and 3(b), without LLD). These dynamic instabilities disappear when referenced atomic positions are relaxed (with LLD), suggesting a stabilization effect associated with LLD, consistent with findings for related bcc HEAs in Ref. [20]. Second, the dynamical instabilities disappear at the highest Nb concentrations (*i.e.*, $x = 50$ at.% in Fig. 3).

We focus next on the results for the spectral functions shown in Fig. 3. For the case with ideal lattice positions (without LLD) presented in Fig. 3(a) and 3(c), all systems show pronounced spectral weight associated with imaginary frequencies, with these instabilities being accentuated as the Nb concentration decreases. However, when LLD are taken into account (see Fig. 3(d) and 3(f)), we find that the spectral weight for imaginary frequencies decreases, indicating that the displacements enhance the stability of the bcc structure. Importantly,

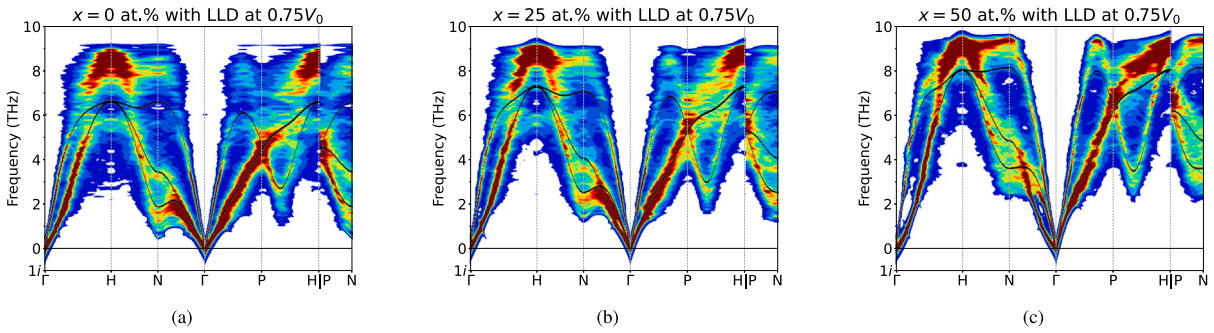

Fig. 4. Pressure effects on atomic vibrations. Calculated dispersion relations for the vibrational spectral functions for bcc $Nb_xTa_{0.25}Ti_{(0.75-x)/2}Hf_{(0.75-x)/2}$ systems, with x equal to (a) 0 at.%, (b) 25 at.% and (c) 50 at.% at $0.75V_0$, where V_0 is the atomic volume at zero pressure. The color map is the same as used in Fig. 3, and the solid lines again indicate phonon dispersions calculated using the VCA. (For interpretation of the references to color in this figure legend, the reader is referred to the web version of this article.)

however, the LLD-induced stabilization is not complete for x equal to 0 and 25 at.% (see Figs. 3(d) and 3(e)), as spectral weight at negative frequencies remains, for example along the 1/2[110] branch (N–point) and between the 1/2[111] and 1/2[110] directions (P–N branch).

A comparison of Figs. 3(d)–3(f) highlights the important role of composition in stabilizing the bcc structure. Specifically, the weight of the spectral functions corresponding to imaginary frequencies decreases with increasing Nb content (x), becoming absent (apart from some remaining weight near Γ) for $x = 50$ at.%. In the supplementary materials we include calculated unfolded phonon dispersion curves for all eleven compositions between $x = 0$ and 50 at.%, finding that this stabilization occurs for $x > 30$ at.%.

At long wavelengths, dynamic stability can be studied in the elastic limit where acoustic frequencies can be written as a linear combination of elastic constants: $v^2 \propto \sum C_{ij}\,\mathbf{k}_i\mathbf{k}_j$ [54]. In a bcc crystal, the tetragonal shear modulus C' is the relevant material property governing the slope of the 1/2[110] branch [36]. The observed trends in the calculated C' (see Fig. 1) agree well with computed phonon dispersions; in particular we observe a pronounced increase in C' with increasing Nb concentration consistent with the stiffening frequencies in the long wavelength limit along this direction shown in Fig. 3.

We note that although C' is positive for $x = 0$ and 25 at.%, we compute a small spectral weight for imaginary frequencies along the 1/2[110] direction, which is most pronounced near the N-point. The behavior is in contrast to the behavior at a $Ti_{0.5}Hf_{0.5}$ composition, where a negative value of C' is associated with an entire unstable branch (see supplementary materials) that reflects instability with respect to a displacive transformation towards the ω phase.

We consider next phonon broadening *i.e.*, the distribution of the spectral weight for a given $\mathbf{k}$. For the $Ta_{0.25}Ti_{0.375}Hf_{0.375}$ composition (see Fig. 3(d)) the spectral function shows a "phonon band gap" near the H-point associated with two different peaks in the spectral function separated by ≈ 2 THz. As described further below, this phonon band gap is a result of the mass difference between the species, as discussed for similar alloys in Ref. [19], due to the fact that the atomic mass of Ta and Hf are much higher than Ti. The band gap shrinks as the Nb concentration increases once the spatial mass distribution becomes more homogeneous.

More generally, the broadening of phonons due to mass fluctuations can be understood with reference to the Klemens model [56], which defines a mass scattering parameter (f_m) of lattice vibrations as: $f_m = \sum_n c_n \left(m_n - \bar{m}\right)^2 / \bar{m}^2$, where c_n and m_n are respectively the concentration and atomic mass of the n–th specie, and $\bar{m}$ is the system average atomic mass. The scattering parameter is equal to 0.24 and 0.16 when the Nb concentration is 0 and 50 at.%, respectively. This decrease in the scattering parameter correlates with the reduction in the extent of phonon broadening with increasing Nb content shown in Fig. 3. The phonon band gap is only clearly observed when LLD are taken into account. The phonon dispersions obtained using ideal lattice sites correspond to an unphysical state and do not properly reflect phonon broadening. The absence of the phonon band gap in Fig. 3(a) is possibly an artifact of such an idealized state.

In principle, phonon broadening associated with dynamical instabilities should arise from fluctuations in the force constants. To explore the relative importance of the force-constant and mass disorder, we examine the role of pressure on the calculated phonons. Applied pressure is expected to stiffen the force constants by a degree that depends on bond type and thus should impact force-constant fluctuations, while leaving the mass fluctuations unchanged. Specifically, in Fig. 4 we present calculated phonons for a compressed volume of $0.75V_0$, where V_0 denotes the equilibrium atomic volume corresponding to the results in Fig. 3. Such volume compression mimics hydrostatic pressures of 58, 68 and 77 GPa for $x = 0$, 0.25 and 0.5, respectively.

The finite-pressure results in Fig. 4 show two noteworthy results. The first is that pressure suppresses the dynamic instabilities reflected by the imaginary frequencies in Fig. 3. This is to be expected for positive values of the Grüneisen parameter $\gamma = -\partial \ln \nu / \partial \ln V$. An analogous behavior is reported in the literature in elemental-crystals, with pressure being correlated to a phonon stiffening observed in fcc tungsten under compression as an illustrative example [57]. We therefore conclude that force fluctuations are the origin of the appearance of spectral weight at imaginary frequencies, corresponding to dynamic instabilities. In this sense, broadening of the frequency range for the spectral functions to low and imaginary frequencies is concluded to be dominated by force-constant fluctuations.

By contrast, the characteristics of broadening associated with the appearance of the phonon band gap appears to arise primarily from mass fluctuations. Specifically, we note in both the calculations at V_0 (Fig. 3) and $0.75V_0$ (Fig. 4) the presence of a phonon band gap of ≈ 2 THz at $x = 0$ at.%, which vanishes at $x = 50$ at.%.

As a final noteworthy result from the calculations discussed in this section, we find that the main features of the phonon spectra are not appreciably affected by the details of the atomic configurations across different SQS models employed in the computations. Specifically, for $x = 0$ at.% (*i.e.*, the $Ta_{0.25}Ti_{0.375}Hf_{0.375}$), we have computed the spectral functions for the configurations giving the smallest and largest values of the LLD. The results are very similar, as demonstrated in the supplementary materials Fig. S2, indicating that phonon dispersions and thus the energy landscape are essentially a function of the composition regardless of either the magnitude of lattice distortions or spatial chemical distribution. We recall that this behavior is also observed for the calculated elastic moduli. This result is supported by previous work which demonstrated that random structures and structures showing B2-type short-range ordering (SRO) for a fixed HEA composition leads to almost identical phonon spectra [19]. In addition, Ref. [20] also showed that phonon dispersion curves of different SQS and Monte Carlo optimized (*i.e.*, showing some degree of SRO) configurations exhibits the same major features.

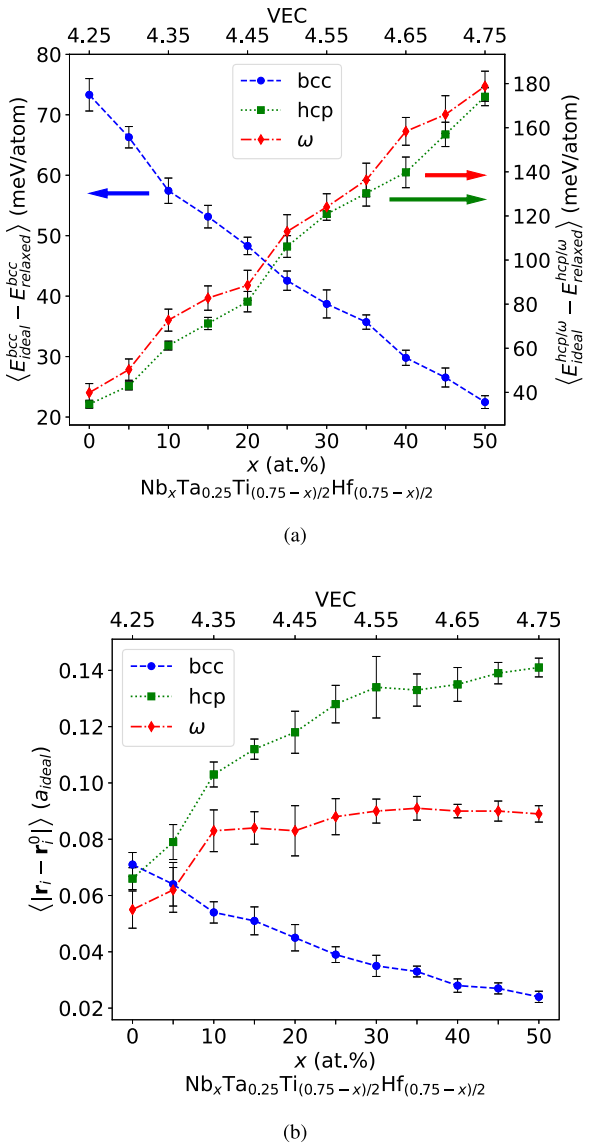

Fig. 5. Averaged values over twenty different SQS models for each phase and composition of the (a) relaxation energy and (b) norm of atomic displacements of phases bcc (blue circles), hcp (green squares) and ω (red diamonds) of $Nb_xTa_{0.25}Ti_{(0.75-x)/2}Hf_{(0.75-x)/2}$ systems. Error bars indicate the variance. In (a), note that the relaxation energy of hcp and ω phases is presented using a different scale. In (b), note that the magnitude of LLD is normalized by the correspondent ideal lattice parameter for each phase and composition. (For interpretation of the references to color in this figure legend, the reader is referred to the web version of this article.)

3.4. Relaxation energies and structural energy differences

We consider next the energetic stability of the bcc structure with reference to the structural energy differences between the bcc, hcp and ω structures, as well as phase separation into constituent elements or unmixing. The formation energy (ΔE_{form}) for a bcc alloy with a given composition $Nb_xTa_{0.25}Ti_{(0.75-x)/2}Hf_{(0.75-x)/2}$ is defined in terms of its energy (E_{bcc}) by the relation: $\Delta E_{\text{form}} = E_{\text{bcc}}(x) - x\,E_{\text{bcc}}(\text{Nb}) - 0.25\,E_{\text{bcc}}(\text{Ta}) - (0.75-x)/2\,E_{\text{hcp}}(\text{Ti}) - (0.75-x)/2\,E_{\text{hcp}}(\text{Hf})$, and represents the energy to form the bcc alloy from pure Nb, Ta, Ti and Hf in the bcc (Nb, Ta) and hcp (Ti and Hf) structures. Similarly, the mixing energy (ΔE_{mix}) is defined as: $\Delta E_{\text{mix}} = E_{\text{bcc}}(x) - x\,E_{\text{bcc}}(\text{Nb}) - 0.25\,E_{\text{bcc}}(\text{Ta}) - (0.75-x)/2\,E_{\text{bcc}}(\text{Ti}) - (0.75-x)/2\,E_{\text{bcc}}(\text{Hf})$, and represents the energy to mix the alloy on a bcc lattice. We analyze twenty different SQS representing various chemical arrangements for each phase and composition.

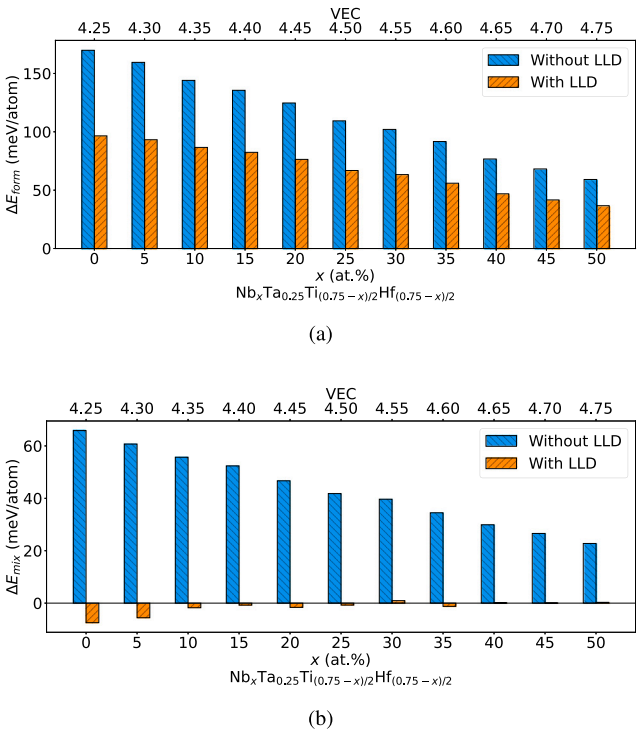

Fig. 6. Calculated (a) formation energies (ΔE_{form}) and (b) mixing energies (ΔE_{mix}) for $Nb_xTa_{0.25}Ti_{(0.75-x)/2}Hf_{(0.75-x)/2}$ with and without LLD as a function of composition (x). The calculated values make use of bcc energies for the alloys averaged over twenty SQS models for each composition.

Figs. 5(a) and 5(b) show respectively the averaged relaxation energy and the norm of the LLD when the structures with compositional disorder are relaxed, starting from the reference ideal bcc, hcp and ω structures. The relaxation energy of a given structure is defined as the energy difference between the cases with and without LLD, taking the first one as reference. With such convention, relaxation energies are always positive, and their magnitude reflects the energetic driving force for distortions away from the ideal reference lattices. We note that the relaxation energy scale for hcp and ω structures is much greater than for bcc. Further, we note that the trend in relaxation energies *versus* composition is opposite for hcp and ω structures *versus* bcc, with the former (latter) increasing (decreasing) in magnitude with increasing x.

The effects of LLD on the formation and mixing energies of the Nb–Ta–Ti–Hf alloys are plotted in Fig. 6. Fig. 6(a) shows that accounting for LLD *i.e.*, accounting for the relaxation energy of the bcc phase, significantly decreases the tendency for phase separation into the constituent hcp and bcc elemental constituents. Specifically, the magnitudes of ΔE_{form} decrease by about 60% with lattice relaxations, to values that would enable these alloys to be stabilized with respect to the phase-separated state by an ideal configurational entropy at temperatures above approximately 1030, 560 and 350 K for $x = 0$, 0.25 and 0.5, respectively.

Considering also the mixing energy results in Fig. 6(b), we see that without LLD the values have positive values for all x. The effect of relaxations is to reduce the values of ΔE_{mix} to small magnitudes very near the ideal mixing limit of zero. Thus, although the lattice relaxations lead to a structurally more complex alloy due to the presence of LLD, they lead to a more ideal alloy in terms of mixing properties.

We consider next the energetic stability of the bcc structure relative to hcp and ω phases. Specifically, we plot in Fig. 7 results for the energy differences among these three structures, considering twenty different SQS models for each phase at each composition. The spread in energy across these structures are indicated with box plots with the median

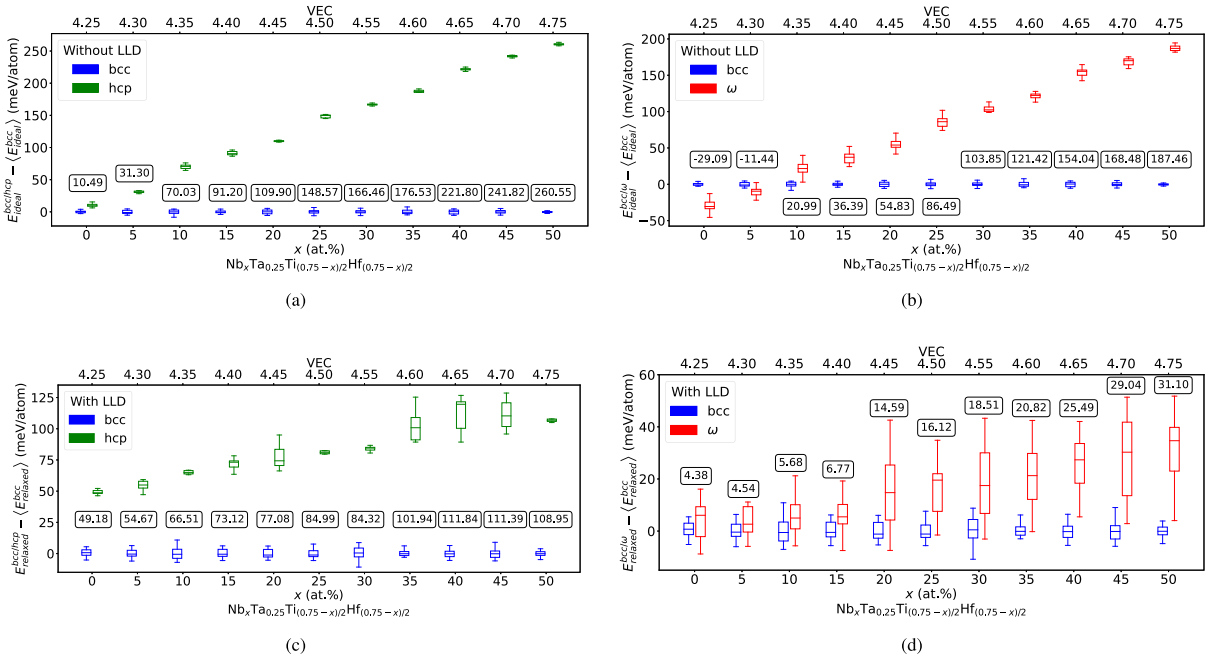

Fig. 7. Calculated structural energy differences for Nb$_x$Ta$_{0.25}$Ti$_{(0.75-x)/2}$Hf$_{(0.75-x)/2}$ systems. Box plots of the difference between the energies of bcc (blue) and hcp/ω (green/red) phases considering structures with atoms constrained to reside on ideal lattice sites (without LLD) in (a) and (b), and accounting for the ionic relaxation of these structures (with LLD) in (c) and (d). Annotated values throughout indicate the difference between the averages of respective energy distributions, taking the bcc structure as reference. A total of twenty different SQS configurations are used for each phase and composition. (For interpretation of the references to color in this figure legend, the reader is referred to the web version of this article.)

energy for each structure and composition indicated by the horizontal lines, and the difference between the averages of respective energy distributions relative to bcc at each composition indicated by annotated values.

Results are plotted in Fig. 7 both excluding (panels a and b) and including (panels c and d) the contributions from structural relaxations, in order to highlight the role of the LLD. Whereas LLD enhance the stability of the bcc phase at low Nb concentrations (x), they lower the magnitude of the structural energy differences between bcc *versus* hcp and bcc *versus* ω, as x increases beyond 0.1. The most important effect of LLD is seen to be for the bcc *versus* hcp structural energy differences. Overall the results highlight the importance of including consideration of LLD in calculations of relative structural stability, as pointed out for related alloys in Ref. [17].

The results in Fig. 7(c) clearly demonstrate the stability of the bcc structure relative to hcp, since the average energies for the latter are higher and there is no overlap in the distributions across the different considered SQS models. By contrast, the results in Fig. 7(d) indicate that in the case of the ω phase a clear conclusion regarding the energetic preference of the bcc structure is possible only when x is larger than 20 at.%. Indeed, at low Nb concentrations the statistical distribution of bcc and ω phases almost fully overlap. This result may be important for activation of transformation-induced plasticity (TRIP) [16,17,58,59] mechanism, such that the results in Fig. 7(d) showing compositions where the energies of ω and bcc are close may provide guidelines for metastability alloy design.

The results in Fig. 7 show that the bcc phase is energetically stable relative to ω for all configurations only for intermediate and higher Nb concentrations. This is qualitatively consistent with the phonon results in Section 3.3, which show that increasing Nb content decreases the presence of spectral weight at imaginary frequencies associated with the transformation of the bcc structure towards a hexagonal lattice.

The valence electron concentration (VEC) *i.e.*, the average number of valence s and d electrons per atom, has been used to compare the structural stability between the bcc and fcc phases in Cantor HEAs [60–62] and is well-known to correlate with structural stability for fcc, bcc, hcp and ω phases in elemental transition metals [63]. We thus include the VEC along with the composition variable x in the plots throughout this work.

In the case of the Nb–Ta–Ti–Hf systems considered here, this parameter is expected to provide only qualitative correlations, showing a trend towards increasing stability of the bcc structure with increasing VEC. It is shown in Refs. [64,65] that significant charge transfer accompanies local relaxations in bcc HEAs. We find similar charge transfer effects, primarily between Ta, Ti and Hf atoms in the systems studied here, and important reconstruction of the d-project DOS, which are most pronounced for the lower values of x, as shown in supplementary materials Figs. S4 and S5. In this way, since theory of stability based solely on VEC is justified by rigid band models, these assumptions become inconsistent with charge transfer effects and electronic structure reorganization described above.

Further, Ti, Zr and Hf belong to the same chemical group, and thus have the same VEC. Nevertheless, the energetics associated with transformation of the bcc structure is significantly different across these three elements [35,50]. For instance, at the elastic limit where the tetragonal shear modulus reflects the instability of the bcc structure, we compute C' values of −3, −9 and −20 GPa in pure bcc Zr, Ti and Hf, respectively. These results highlight that the role of group IV elements in governing stability of the bcc lattice is generally expected to differ between Ti, Zr and Hf despite them having the same VEC.

3.5. Local lattice distortions (LLD)

We consider in this section the calculated LLD. We start by presenting the magnitude of these displacements in the first subsection, and move to consider the nature of the LLD in relation to ω and hcp transformation pathways subsequently. We then focus on ω-like distortions in the bcc lattice, discussing the energy landscape underlying these distortions as well as compositional effects.

3.5.1. LLD magnitudes and atomic misfit versus composition

The magnitudes of the calculated LLD are presented in Fig. 5(b) which plots *versus* x the quantity $\langle|\mathbf{r}_i - \mathbf{r}_i^0|\rangle$: the norm of atomic displacements averaged over all atoms of a given configuration, across twenty SQS configurations for a given composition, where $\mathbf{r}_i$ and $\mathbf{r}_i^0$ denote the coordinates of the i–th atom at relaxed and ideal lattice positions, respectively. The magnitudes of the LLD calculated in the bcc structure monotonically decrease with increasing x, contrary to the hcp and ω structures where the displacements initially increase in magnitude with x and then continue to grow at a slower rate. While the hcp structure shows the largest lattice distortions (normalized by the respective lattice parameter) from medium up to high Nb concentrations, the ω phase shows slightly smaller magnitudes and plateaus at intermediate values of x. Over this concentration range, the most important contribution of atomic displacements observed in the ω phase comes from the high distortion of the atoms that are located in the basal planes of this structure, corresponding to about 85% of the LLD magnitudes, which indicates a spontaneous reconstruction towards the bcc structure. Due to cell geometry constrains of the hcp phase, we do not observe a clear structural reorganization of the structure towards bcc even at high Nb concentrations. A detailed analysis of the displacements for the bcc phase is presented in the next subsection.

The magnitude of LLD observed in the bcc phase may provide insightful guidelines for alloy design, with respect to controlling strength *versus* ductility relations. Whereas chemical complexity induces the formation of cross-kinks in screw dislocations leading to extra strength [66,67], large LLD in the bulk have been observed in simulations to correlate with decreasing disparity between the mobility of edge and screw dislocations [68,69], which has been suggested to be a factor underlying improvements in ductility [69]. As shown in Fig. 5(b), a large concentration of group IV elements allows to maximize LLD observed in the bcc phase, and correlates with the known improvement of room-temperature ductility in the group IV containing Senkov alloys [5,7,21] compared to the refractory bcc HEAs (*e.g.*, NbTaMoW [4]) composed of group V and VI elements alone. A LLD informed ductility criterion is presented in Ref. [70], which correlates well with experimental observations. Although models based on VEC have also shown guidelines in describing brittle *versus* ductile alloys [71], use of LLD informed ductility criteria are viewed to be better justified theoretically given that the lattice distortions are coupled with charge-transfer and electronic structure changes that are beyond the rigid band models that typically underlie predictions based solely on VEC. We note that the large magnitudes for LLD obtained here have been measured experimentally in other group IV enriched bcc HEAs [64], and are computed to be more than five and three times larger than fcc and other bcc HEAs [20,72], respectively.

We consider further the atomic volume misfit across the compositions considered in this work. The importance of this parameter in the context of the solid-solution strengthening effect for edge dislocations in HEAs has been highlighted in previous theoretical work [73,74]. A broadly-used normalized misfit parameter δ_{misfit} is defined as $\delta_{\text{misfit}} = \sqrt{\sum_n c_n \Delta V_n^2 / 9\bar{V}^2}$ [74], where c_n and ΔV_n are respectively the concentration and misfit volume relative to the average atomic volume ($\bar{V}$) of the n–th specie. We consider two different scenarios to calculate the misfit parameter: (i) using a concentration-weighted sum of the elemental atomic values to compute $\bar{V}$ (*i.e.*, Vegard's Law [75,76]), and (ii) using a Bader charge analysis [77] and accounting for LLD, where the misfit parameter is calculated in terms of Bader atomic volumes. The second method is introduced as it enables an assessment of how charge transfer affects atomic misfit. Details on the Bader analysis can be found in the supplementary materials. Table 3 lists the values of $\bar{V}$ and δ_{misfit} calculated by these two methods.

Table 3 shows that $\bar{V}$ obtained *via* the Bader analysis (method (ii)) is consistent with the alloy equilibrium volumes calculated using the EOS (aside from numerical errors $< 10^{-3}$ Å^3), and that the Vegard's Law (method (i)) slightly overestimates $\bar{V}$ by 1% maximum at $x = 0.25$. The difference in the results provided by methods (i) and (ii) is more evident in the obtained misfit parameters. Specifically, method (ii) leads to significantly larger values of δ_{misfit} due to the related LLD and charge transfer effects noted earlier. Moreover, whereas the Vegard's Law analysis provides a monotonous relation between the Nb concentration and misfit parameter, the Bader analysis shows a nonlinear correlation at lower and intermediate Nb content, highlighting the role of charge transfer effects on atomic misfit calculated by method (ii). While it is not clear which of these different methods give values that are most relevant to increasing strength, the differences point to potential limits of employing estimates based solely on alloy composition (*i.e.*, method (i)).

Table 3
Average atomic volume ($\bar{V}$) and misfit parameter (δ) of bcc $Nb_xTa_{0.25}Ti_{(0.75-x)/2}Hf_{(0.75-x)/2}$ systems calculated according to two different scenarios outlined in the text, based on (i) volumes of the bcc pure elements (Vegard's Law [75,76]), and (ii) an analysis based on Bader volumes.

x	$\bar{V}$ (Å^3/atom)		δ_{misfit} (%)	
(at.%)	(i)	(ii)	(i)	(ii)
0	19.13	19.05	4.0	6.5
5	19.10	18.98	3.9	6.2
10	19.01	18.88	3.7	5.9
15	18.97	18.81	3.6	6.4
20	18.93	18.80	3.5	6.0
25	18.86	18.68	3.3	5.2
30	18.80	18.66	3.2	5.1
35	18.76	18.61	3.1	4.9
40	18.67	18.55	2.8	4.6
45	18.63	18.53	2.7	4.2
50	18.60	18.50	2.5	4.1

3.5.2. Nature of displacements in the bcc phase

We investigate next the nature of the LLD in relation to the displacements towards the ω and hcp structures. Specifically, we employ an analysis involving the projection of the lattice displacements onto known structural transformation paths for these phases. Such a framework was first proposed to detect a bcc→ω transformation in pure Ti in Ref. [78], and then modified to analyze the structural stability of group IV enriched bcc HEAs in Refs. [17,18].

We recall that the ω phase can be obtained from the bcc structure through correlated displacements of $\{111\}_{\text{bcc}}$ lattice planes, as illustrated in Fig. 8(a). Specifically, along the $1/2\langle 111\rangle_{\text{bcc}}$ direction, the bcc structure shows an ABC stacking, with an interplanar spacing of $\sqrt{3}/6\, a_{\text{bcc}}$, where a_{bcc} is the lattice constant of the parent bcc structure. Thus, the pathway for the bcc→ω transformation can be described by one parameter, δ_ω defined as in Fig. 8(a), where 1/3 of the $\{111\}_{\text{bcc}}$ planes remain undisplaced while the other 2/3 collapse onto a common plane. The total atomic displacement to accomplish a full transformation is: $\delta_\omega = \sqrt{3}/12\, a_{\text{bcc}}$. We can thus define a structural descriptor based on the projection of the atomic displacements onto this transformation path as follows:

1. Calculate atomic displacements of optimized structures with respect to ideal bcc lattice sites.
2. Project these displacements along the four independent $\langle 111\rangle_{\text{bcc}}$ directions.
3. Compute the projected amplitudes (*i.e.*, the norm of the projected displacements) along each direction and then average them over all atoms in the cell.
4. Sort the obtained values such that they take form as $\{p_1, p_2, p_3, p_4\}$, where p_1 is the largest.
5. Evaluate $p_1 - p_2$ to distinguish the structural transformation from random, uncorrelated LLD.
6. Normalize $p_1 - p_2$ by δ_ω to allow a comparison across different compositions.

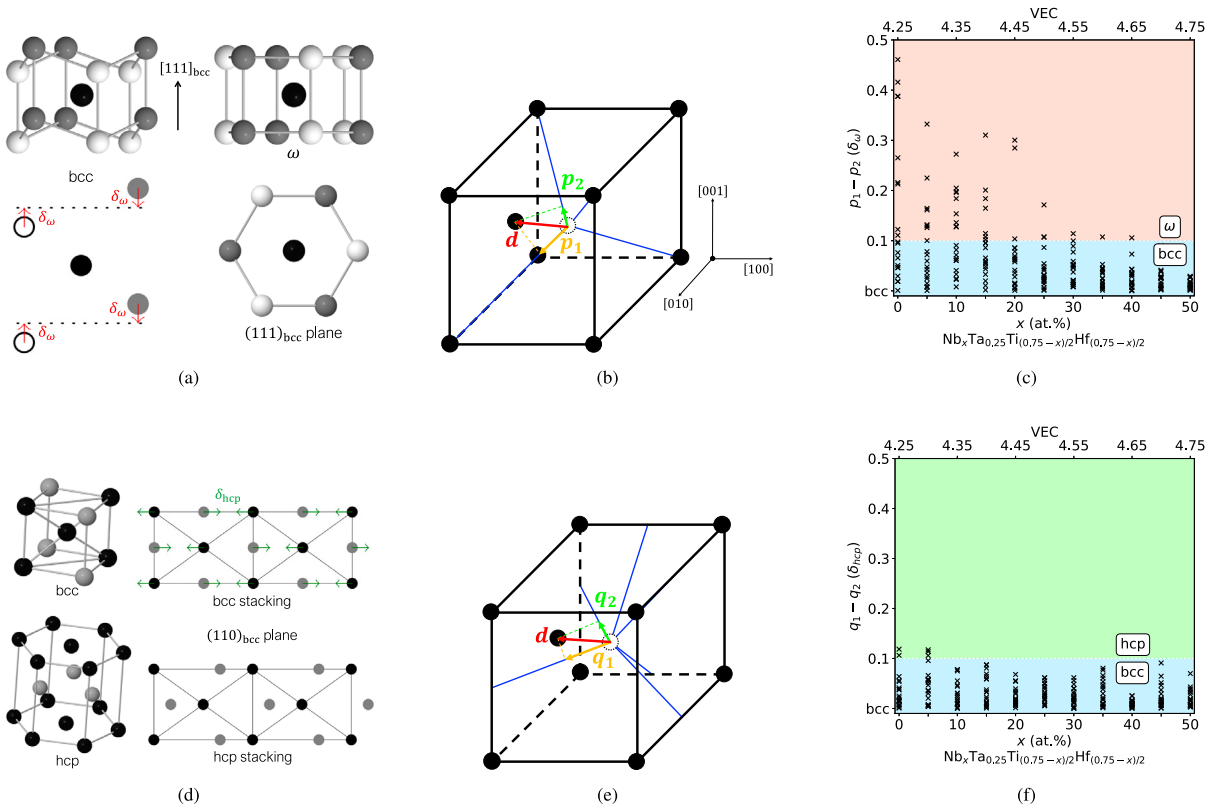

Fig. 8. Relationship between displacements in the bcc structure and transformations to ω and hcp. Schematic representation of the (a) bcc→ω transformation and (d) alternating slide displacement of $\{110\}_{bcc}$ planes yielding to an hcp stacking along this same direction. Illustration of the structure descriptor used to detect the transformation of the bcc structure towards the (b) ω and (e) hcp phases. Descriptors are built based on atomic displacements projected along the transformation path reaction coordinate. Calculated values of the ω and hcp descriptors for $Nb_xTa_{0.25}Ti_{(0.75-x)/2}Hf_{(0.75-x)/2}$ systems are plotted in panels (c) and (f), respectively. Each cross in (c) and (f) corresponds to a different SQS configuration, relaxed from an initial state with atoms located at ideal bcc positions. A total of twenty SQS configurations are considered for each composition.

Fig. 8(b) illustrates the definition of the structure descriptor. According to its formulation, $p_1 - p_2\,(\delta_\omega)$ is equal to 0 or 1 when a given structure is ideal bcc or ω, respectively. Step 5 is key in the case of HEAs since, regardless of structural reconstruction, atomic positions can feature substantial deviations from ideal lattice sites arising from chemical disorder. Nevertheless, for the case where displacements reflect transformation towards the ω phase, the projection described above, along the symmetry-broken $\langle 111\rangle_{bcc}$ direction should be appreciably larger, allowing to identify such structural transformations [17].

The tetragonal Burgers path, connecting the bcc to the hcp phase, is defined in terms of two parameters: a lattice shearing corresponding to C' (see above) and an alternating displacement of $\{110\}_{bcc}$ planes resulting from phonon modes along the 1/2[110] branch [42,49]. We focus here on the shuffle which is schematically presented by Fig. 8(d). The total magnitude of the atomic displacement leading to hcp AB stacking along $1/2\langle 110\rangle_{bcc}$ is given by: $\delta_{hcp} = \sqrt{2}/12\,a_{bcc}$. Following an approach similar to that described above for bcc→ω, we can define a structure descriptor to detect distortions reflecting the bcc→hcp transformation. Specifically, in step 2, we consider the six independent $\langle 110\rangle_{bcc}$ directions as illustrated by Fig. 8(e), with the resulting averaged projected amplitudes labeled as q_1 through q_6, similar to step 4. Further, in step 6 the normalization parameter becomes δ_{hcp}. Analogous to $p_1 - p_2\,(\delta_\omega)$, the descriptor $q_1 - q_2\,(\delta_{hcp})$ is equal to 0 or 1 when a given structure shows ideal bcc or hcp stacking along $1/2\langle 110\rangle_{bcc}$, respectively.

Fig. 8(c) displays the computed bcc→ω descriptors across all considered $Nb_xTa_{0.25}Ti_{(0.75-x)/2}Hf_{(0.75-x)/2}$ compositions, considering twenty different configurations for each x. At low Nb concentrations, the structural descriptor $p_1 - p_2$ shows a broad range of values across the twenty individual configurations, with magnitudes as large as 0.45. These results indicate that some configurations show structural distortions consistent with transformation significantly towards the ω phase. From medium up to high Nb concentrations, the number of structures showing large magnitudes for this structural descriptor significantly decreases, indicating an enhancement of the stability of the bcc lattice. Given the phonon and structural energy results presented in Sections 3.3 and 3.4, respectively, we identify that a Nb concentration greater than 30 at.% corresponds to a complete stabilization of the bcc structure. For $x > 30$ at.%, Fig. 8(c) shows that only two SQS configurations have $p_1 - p_2$ values (slightly) greater than 0.1. We therefore set $p_1 - p_2\,(\delta_\omega) = 0.1$ to classify the local atomic structures in two groups: bcc- and ω-like. We remark that the employed criterion of $p_1 - p_2\,(\delta_\omega) = 0.1$ to discriminate the structures is different than Ref. [17], partly due to our chosen normalization parameter (δ_ω), and also the results described above.

A similar analysis for $q_1 - q_2$ does not show evidence of a significant bcc→hcp structural reconstruction for any of the configurations at any of the compositions, as shown in Fig. 8(f). We employ the same threshold of 0.1 as used for ω distortions, also for $q_1 - q_2$ in the plot in order to highlight that relaxed bcc structures show little evidence of distortions towards to hcp, in comparison to what is found for ω. Thus, neither the shuffle nor the tetragonal shear (see Fig. 2) associated with hcp transformation are reflected in the relaxed configurations and energy *versus* strain relations, respectively. These results are consistent with the large energy difference separating bcc and hcp phases (see Fig. 7(c)).

3.5.3. Energy landscape underlying ω distortions

We consider further the bcc *versus* ω competition, noting that for low Nb concentrations Fig. 8(c) shows a wide range of values for the quantity $p_1 - p_2$ corresponding to different quasirandom configurations. This configurational dependence stands in contrast to the elastic and

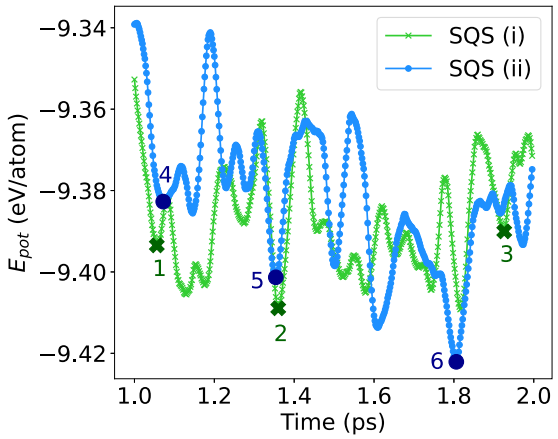

Fig. 9. Potential energy (E_{pot}) *versus* time recorded during the AIMD trajectories at 1300 K of two different SQS configurations (shown by different colors and markers) for $Ta_{0.25}Ti_{0.375}Hf_{0.375}$. (For interpretation of the references to color in this figure legend, the reader is referred to the web version of this article.)

Table 4
Computed structural bcc→ω descriptors ($p_1 - p_2$) and relative energy differences (ΔE) of structures obtained by energy relaxation at zero temperature, starting from the different initial states indicated in Fig. 9. The reference configuration (Ref.) used to compute ΔE is the initial snapshot of the AIMD simulation (*i.e.*, t = 0 ps), corresponding to atomic positions obtained upon the relaxation of ideal bcc lattice sites.

SQS	Snapshot	$p_1 - p_2$ (δ_ω)	ΔE (meV/atom)
(i)	Ref.	0.28	–
	#1	0.42	<1
	#2	0.13	<1
	#3	0.21	<1
(ii)	Ref.	0.03	–
	#4	0.01	<1
	#5	0.40	<1
	#6	0.20	<1

dynamic stability which, as discussed above, showed little variation across the different SQS structures.

To gain further insight into this result, we investigate the potential energy landscape, focusing specifically on the $Ta_{0.25}Ti_{0.375}Hf_{0.375}$ (*i.e.*, $x = 0$ at.%) system. Specifically, we perform *ab initio* molecular dynamics (AIMD) simulations on two different SQS models for this ternary alloy, namely those which display high and low values of $p_1 - p_2$ in Fig. 8(c). The systems are brought to high temperature (T = 1300 K) and we record the evolution of the potential energy (E_{pot}) explored by the system through thermal fluctuations (details of the simulations can be found in the Methods section).

Fig. 9 plots the potential energy *versus* time during the AIMD trajectory. We select several snapshots from the trajectory for each SQS, and then these configurations are structurally relaxed at zero temperature. As shown in Table 4, the calculated energy differences between these relaxed snapshots, and their reference configuration represented in Fig. 8(c) (obtained from energy minimization starting with ideal bcc coordinates) are less than 1 meV/atom. However, all computed bcc→ω descriptors (*i.e.*, $p_1 - p_2$) are different in magnitude, being either larger or smaller than the corresponding values in the reference configuration. Moreover, we verify that this same behavior is observed not only considering local minima of the potential energy but also in snapshots that are just a few time-steps apart (see supplementary materials). Optimized atomic positions obtained upon ionic relaxation are thus strongly influenced by the initial starting displacements.

We therefore conclude that the multidimensional energy landscape features multiple, nearly energetically degenerate local minima. Some of them corresponding to nearly uncorrelated LLD, with others showing pronounced correlated distortions towards the ω phase, as reflected in the larger values of $p_1 - p_2$.

3.5.4. Compositional effects on ω distortions in the bcc lattice

We focus next on the compositional effects on the ω-like distortions discussed above, and the associated relaxation energies. Due to the presence of the group V elements (Nb and Ta), the observed intrinsic instabilities in the bcc lattice are weaker than in pure group IV alloys (see Section 3.3), such that they cannot lead to a perfect alternate collapse of $\{111\}_{bcc}$ planes (*i.e.*, a complete bcc→ω transformation) such as we have observed in relaxations in binary bcc $Ti_{0.5}Hf_{0.5}$. Indeed, the greatest $p_1 - p_2$ obtained among all of the bcc $Nb_xTa_{0.25}Ti_{(0.75-x)/2}Hf_{(0.75-x)/2}$ HEAs considered here represents less than 50% of the bcc→ω reconstruction. We also show that increasing Nb concentration induces appreciable changes on the energy landscape such that atomic arrangements corresponding to energy minima become closer to ideal bcc lattice sites, reflected by their smaller magnitude of LLD (see Fig. 5(b)) and low variation of $p_1 - p_2$ (see Fig. 8(c)).

We propose that, more generally, lattice distortions observed in the bcc $Nb_xTa_{0.25}Ti_{(0.75-x)/2}Hf_{(0.75-x)/2}$ systems do not merely reflect the atomic and elastic misfit of accommodating the different chemical species [12,13], but correlate with a competition between two effects: (i) a driving force for bcc→ω transformation which arises from the Ti-Hf bonding preferences, and (ii) a shear energy barrier to such transformation induced by the group V elements (Nb–Ta) concentration.

The aforementioned shear resistance is correlated with the shear modulus G_{111} along the $\langle 111\rangle_{bcc}$ direction on the $\{112\}_{bcc}$ plane, associated with the collapse mechanism of the bcc→ω transformation [59,79]. G_{111} can be computed using the elastic constants obtained for the bcc structure such that: $G_{111} = (3 \times C_{44} \times C')/(2\,C_{44} + C')$ [42,80]. As such, G_{111} is closely related to the tetragonal shear modulus, showing the same trends as observed for C' presented in Fig. 1. Specifically, G_{111} is always positive for all bcc $Nb_xTa_{0.25}Ti_{(0.75-x)/2}Hf_{(0.75-x)/2}$ systems, indicating a shear energy barrier opposing the bcc→ω transformation.

Moreover, G_{111} shows pronounced stiffening with increasing Nb concentration, with G_{111} rising from 29 to 44 GPa for x equal to 0 and 0.5, respectively (see supplementary materials). We note that a similar intrinsic competition between a bcc→ω transformation driving force *versus* a shear energy barrier has been proposed in the literature to explain the partially collapsed ω phase observed in metastable bcc Ti-Nb [58] and Ti-Mo [59] alloys.

We investigate next the energy landscape along the bcc→ω transformation of binary $Ti_{0.5}Hf_{0.5}$, as shown by black circles in Fig. 10. We use the $p_1 - p_2$ descriptor to indicate the reaction coordinate along the transformation path. As such, the atomic arrangement corresponds to ideal bcc lattice sites when $p_1 - p_2\,(\delta_\omega) = 0$, and perfect ω lattice positions when $p_1 - p_2\,(\delta_\omega) = 1$. Images (*i.e.*, intermediate configurations) along the transformation path are obtained using linear interpolation. The energetic driving force is computed by performing frozen DFT calculations (no constrained optimization is employed). Fig. 10 highlights that the bcc→ω transformation for $Ti_{0.5}Hf_{0.5}$ is spontaneous, showing no energy barrier, as found for similar calculations in pure bcc Ti and Hf [50].

To elucidate the proposed competition mechanism presented above to describe the nature of the LLD observed in our studied HEAs, we juxtapose in Fig. 10 on the plot for $Ti_{0.5}Hf_{0.5}$, the maximum $p_1 - p_2$ and relaxation energy at each composition for bcc $Nb_xTa_{0.25}Ti_{(0.75-x)/2}Hf_{(0.75-x)/2}$ systems (from Fig. 8(c)). For clarity, we use here the ideal bcc structure as reference to compute the relaxation energy such that it has opposite sign relative to the convention used in Section 3.4.

Fig. 10 shows that at $x = 0$ at.%, and at the same energy coordinate, the maximum observed $p_1 - p_2$ (see Fig. 8(c)) in the HEAs is very close to the correspondent reaction coordinate of the $Ti_{0.5}Hf_{0.5}$ bcc→ω transformation. In other words, in the $Ta_{0.25}Ti_{0.375}Hf_{0.375}$, the bcc→$\omega$

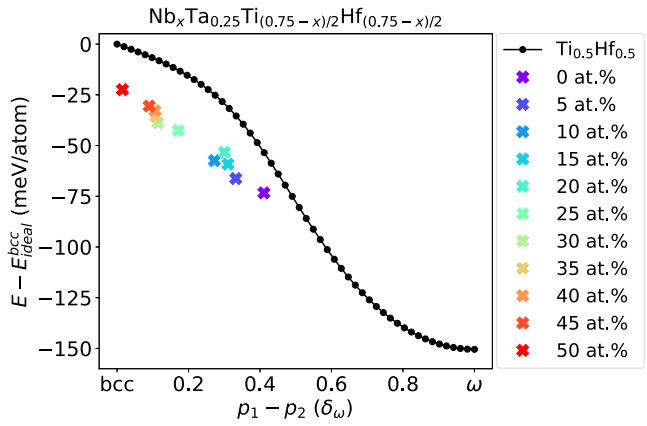

Fig. 10. Composition interplay on ω-like distortion observed in the bcc phase. Black circles denote frozen DFT calculations along the pathway of the bcc→ω transformation of the binary $Ti_{0.5}Hf_{0.5}$. Colored crosses represent maximum $p_1 - p_2$ observed at each composition shown in Fig. 8(c), and the correspondent energetic driving force arising from the relaxation of ideal bcc lattice sites of these structures. The legend box indicates the Nb concentration (x) in bcc $Nb_xTa_{0.25}Ti_{(0.75-x)/2}Hf_{(0.75-x)/2}$ systems. (For interpretation of the references to color in this figure legend, the reader is referred to the web version of this article.)

reconstruction driving force induced by the large Ti-Hf concentration is strong compared to the shear energy barrier induced by 25 at.% of Ta, as reflected by the low G_{111} computed at this composition. With the increasing Nb concentration, again at the same energy coordinate, the separation between the maximum HEAs $p_1 - p_2$ and the corresponding $Ti_{0.5}Hf_{0.5}$ reaction coordinate increases, reflecting the increasing shear energy barrier, which correlates with the observed stiffening of G_{111}. In fact, when the Nb content becomes greater than the critical concentration required for a complete stabilization of the bcc lattice ($x > 30$ at.%, see Section 3.3), Fig. 10 shows that the results for the $Nb_xTa_{0.25}Ti_{(0.75-x)/2}Hf_{(0.75-x)/2}$ no longer shows a correlation with the $Ti_{0.5}Hf_{0.5}$ bcc→ω energy pathway. In this way, we demonstrate that the large magnitudes of LLD observed at low Nb concentrations not only reflect atomic-size and elastic misfit, but also show evidence of a bcc→ω transformation driving force arising from Ti-Hf bonds. This driving force becomes less important as the Nb concentration increases, which combined with the increasing shear resistance to structural change away from the bcc lattice arising from Nb–Ta bonds, results in the smaller magnitudes of LLD observed in the bulk.

4. Summary and conclusions

We present results of DFT calculations for the elastic, dynamic, energetic and structural stability of bcc phases in the Nb–Ta–Ti–Hf HEA system. We consider the effects of varying the ratio of group IV (Ti + Hf) to group V (Nb + Ta) concentrations, through calculations as a function of x in $Nb_xTa_{0.25}Ti_{(0.75-x)/2}Hf_{(0.75-x)/2}$ alloys. We demonstrate the roles of composition and local lattice distortions (LLD) in governing the stability of the bcc phase relative to the competing hcp and ω structures. The main conclusions can be summarized as follows:

- Calculated elastic moduli indicate elastic stability for all values of x between 0 and 0.5, independent of the detailed atomic configurations used in the different special quasirandom structure (SQS) models. Both increasing concentration of group V elements, and the presence of LLD enhance the elastic stability of the bcc structure, as reflected by increasing values of the tetragonal shear modulus.
- The dynamic stability assessement of the bcc structure, analyzed in terms of the phonon spectral functions, shows indications of instabilities associated with the transformation towards a hexagonal lattice for lower and intermediate concentrations of group V elements. These instabilities are qualitatively similar to those obtained in binary bcc $Ti_{0.5}Hf_{0.5}$, but with both LLD and increasing group V content acting to suppress them. No indications of dynamic instability are observed for x greater than 0.3.
- Although the bcc phase is found to be energetically stable for all compositions relative to hcp, the ω phase shows energies close to bcc for lower values of x with the spectra of energies across different SQS configurations overlapping for $x < 0.2$. For larger values of x bcc becomes clearly energetically stable. The effect of LLD is to decrease the magnitude of the structural energy differences, enhancing the stability of the bcc phase for low x, but making the ω phase in particular more energetically competitive for higher concentrations of group V elements.
- The magnitudes of the LLD are calculated to be large (up to an average value of 0.24 Å) in bcc alloys with the highest concentration of group IV elements, and decrease in magnitude to values comparable to other stable HEAs with increasing x. The LLD show signatures of correlated displacements towards the ω phase for x less than approximately 0.3, where we also find a complex energy landscape characterized by multiple nearly degenerate energy minima corresponding to different degrees of ω-like distortions. The degree of ω-like collapses are incomplete for all configurations and compositions considered. No evidence of displacements towards the hcp phase are found.

Overall, the results provide important insights into the ways in which composition can be tuned to control the relative stability of competing phases in bcc Nb–Ta–Ti–Hf alloys, which may have important implications for activating transformation-induced plasticity (TRIP) mechanisms [16,17,58,59]. Additionally, composition is shown to have a strong effect on LLD, the control over which could have important implications for the mobility of edge *versus* screw dislocations [68,69].

Declaration of competing interest

The authors declare that they have no known competing financial interests or personal relationships that could have appeared to influence the work reported in this paper.

Acknowledgments

This work was supported by the US Department of Energy, Office of Basic Energy Sciences, Materials Sciences and Engineering Division under contract No. DE-AC02-05CH11231 as part of the Damage-Tolerance in Structural Materials (KC13) program. This study made use of computational resources of the National Energy Research Scientific Computing Center (NERSC), which is also supported by the Office of Basic Energy Sciences of the US Department of Energy under the same contract number. Additional computational resources were provided at the Pittsburgh Supercomputing Center (PSC) Bridges-2 through allocation No. DMR110087 from the Advanced Cyberinfrastructure Coordination Ecosystem: Services & Support (ACCESS) program, which is supported byNational Science Foundation grants Nos. 2138259, 2138286, 2138307, 2137603, and 2138296.

Appendix A. Supplementary data

Supplementary material related to this article can be found online at https://doi.org/10.1016/j.actamat.2023.119415.

References

[1] O.N. Senkov, G.B. Wilks, D.B. Miracle, C.P. Chuang, P.K. Liaw, Refractory high-entropy alloys, Intermetallics 18 (9) (2010) 1758–1765, http://dx.doi.org/10.1016/j.intermet.2010.05.014.

[2] D.B. Miracle, O.N. Senkov, A critical review of high entropy alloys and related concepts, Acta Mater. 122 (2017) 448–511, http://dx.doi.org/10.1016/j.actamat.2016.08.081.

[3] O.N. Senkov, D.B. Miracle, K.J. Chaput, J.-P. Couzinie, Development and exploration of refractory high entropy alloys – A review, J. Mater. Res. 33 (19) (2018) 3092–3128, http://dx.doi.org/10.1557/jmr.2018.153.

[4] O.N. Senkov, G.B. Wilks, J.M. Scott, D.B. Miracle, Mechanical properties of $Nb_{25}Mo_{25}Ta_{25}W_{25}$ and $V_{20}Nb_{20}Mo_{20}Ta_{20}W_{20}$ refractory high entropy alloys, Intermetallics 19 (5) (2011) 698–706, http://dx.doi.org/10.1016/j.intermet.2011.01.004.

[5] O.N. Senkov, J.M. Scott, S.V. Senkova, D.B. Miracle, C.F. Woodward, Microstructure and room temperature properties of a high-entropy TaNbHfZrTi alloy, J. Alloys Compd. 509 (20) (2011) 6043–6048, http://dx.doi.org/10.1016/j.jallcom.2011.02.171.

[6] W.-C. Hsu, T.-E. Shen, Y.-C. Liang, J.-W. Yeh, C.-W. Tsai, In situ analysis of the Portevin-Le Chatelier effect from low to high-entropy alloy in equal HfNbTaTiZr system, Acta Mater. 253 (2023) 118981, http://dx.doi.org/10.1016/j.actamat.2023.118981.

[7] S. Wang, M. Wu, D. Shu, G. Zhu, D. Wang, B. Sun, Mechanical instability and tensile properties of TiZrHfNbTa high entropy alloy at cryogenic temperatures, Acta Mater. 201 (2020) 517–527, http://dx.doi.org/10.1016/j.actamat.2020.10.044.

[8] S. Jha, A. Sharma, S. Dasari, S. Muskeri, R. Banerjee, S. Mukherjee, Orientation dependent stress-induced martensitic and omega transformations in a refractory high entropy alloy, Materials 28 (2023) 101741, http://dx.doi.org/10.1016/j.mtla.2023.101741.

[9] X. Wen, L. Zhu, M. Naeem, H. Huang, S. Jiang, H. Wang, X. Liu, X. Zhang, X.-L. Wang, Y. Wu, Z. Lu, Strong work-hardenable body-centered-cubic high-entropy alloys at cryogenic temperature, Scr. Mater. 231 (2023) 115434, http://dx.doi.org/10.1016/j.scriptamat.2023.115434.

[10] H. Chen, A. Kauffmann, S. Laube, I.-C. Choi, R. Schwaiger, Y. Huang, K. Lichtenberg, F. Müller, B. Gorr, H.-J. Christ, M. Heilmaier, Contribution of lattice distortion to solid solution strengthening in a series of refractory high entropy alloys, Metall. Mater. Trans. A 49 (3) (2017) 772–781, http://dx.doi.org/10.1007/s11661-017-4386-1.

[11] C. Lee, G. Song, M.C. Gao, R. Feng, P. Chen, J. Brechtl, Y. Chen, K. An, W. Guo, J.D. Poplawsky, S. Li, A. Samaei, W. Chen, A. Hu, H. Choo, P.K. Liaw, Lattice distortion in a strong and ductile refractory high-entropy alloy, Acta Mater. 160 (2018) 158–172, http://dx.doi.org/10.1016/j.actamat.2018.08.053.

[12] I. Toda-Caraballo, P.E.J. Rivera-Diaz-del-Castillo, Modelling solid solution hardening in high entropy alloys, Acta Mater. 85 (2015) 14–23, http://dx.doi.org/10.1016/j.actamat.2014.11.014.

[13] F.G. Coury, M. Kaufman, A.J. Clarke, Solid-solution strengthening in refractory high entropy alloys, Acta Mater. 175 (2019) 66–81, http://dx.doi.org/10.1016/j.actamat.2019.06.006.

[14] H. Huang, Y. Wu, J. He, H. Wang, X. Liu, K. An, W. Wu, Z. Lu, Phase-transformation ductilization of brittle high-entropy alloys via metastability engineering, Adv. Mater. 29 (30) (2017) 1701678, http://dx.doi.org/10.1002/adma.201701678.

[15] L. Zhang, H. Fu, S. Ge, Z. Zhu, H. Li, H. Zhang, A. Wang, H. Zhang, Phase transformations in body-centered cubic NbxHfZrTi high-entropy alloys, Mater. Charact. 142 (2018) 443–448, http://dx.doi.org/10.1016/j.matchar.2018.06.012.

[16] S. Huang, W. Li, E. Holmstrom, L. Vitos, Phase-transition assisted mechanical behavior of $TiZrHfTa_x$ high-entropy alloys, Sci. Rep. 8 (1) (2018) http://dx.doi.org/10.1038/s41598-018-30892-x.

[17] Y. Ikeda, K. Gubaev, J. Neugebauer, B. Grabowski, F. Kormann, Chemically induced local lattice distortions versus structural phase transformations in compositionally complex alloys, npj Comput. Mater. 7 (1) (2021) http://dx.doi.org/10.1038/s41524-021-00502-y.

[18] K. Gubaev, Y. Ikeda, F. Tasnadi, J. Neugebauer, A.V. Shapeev, B. Grabowski, F. Kormann, Finite-temperature interplay of structural stability, chemical complexity, and elastic properties of bcc multicomponent alloys from ab initio trained machine-learning potentials, Phys. Rev. Mater. 5 (7) (2021) http://dx.doi.org/10.1103/physrevmaterials.5.073801.

[19] F. Kormann, Y. Ikeda, B. Grabowski, M.H.F. Sluiter, Phonon broadening in high entropy alloys, npj Comput. Mater. 3 (1) (2017) http://dx.doi.org/10.1038/s41524-017-0037-8.

[20] G.D. Samolyuk, Y.N. Osetsky, G.M. Stocks, J.R. Morris, Role of static displacements in stabilizing body centered cubic high entropy alloys, Phys. Rev. Lett. 126 (2) (2021) http://dx.doi.org/10.1103/physrevlett.126.025501.

[21] H. Chen, T. Hanemann, S. Seils, D. Schliephake, A.S. Tirunilai, M. Heilmaier, K.-P. Weiss, A. Kauffmann, Influence of temperature and plastic strain on deformation mechanisms and kink band formation in homogenized HfNbTaTiZr, Crystals 11 (2) (2021) 81, http://dx.doi.org/10.3390/cryst11020081.

[22] P. Hohenberg, W. Kohn, Inhomogeneous electron gas, Phys. Rev. 136 (3B) (1964) B864–B871, http://dx.doi.org/10.1103/PhysRev.136.B864.

[23] W. Kohn, L.J. Sham, Self-consistent equations including exchange and correlation effects, Phys. Rev. 140 (4) (1965) A1133–A1138, http://dx.doi.org/10.1103/PhysRev.140.A1133.

[24] G. Kresse, J. Furthmüller, Efficient iterative schemes for *ab initio* total-energy calculations using a plane-wave basis set, Phys. Rev. B 54 (16) (1996) 11169–11186, http://dx.doi.org/10.1103/PhysRevB.54.11169.

[25] P.E. Blöchl, Projector augmented-wave method, Phys. Rev. B 50 (24) (1994) 17953, http://dx.doi.org/10.1103/PhysRevB.50.17953.

[26] G. Kresse, D. Joubert, From ultrasoft pseudopotentials to the projector augmented-wave method, Phys. Rev. B 59 (3) (1999) 1758–1775, http://dx.doi.org/10.1103/PhysRevB.59.1758.

[27] J.P. Perdew, K. Burke, M. Ernzerhof, Generalized gradient approximation made simple, Phys. Rev. Lett. 77 (18) (1996) 3865–3868, http://dx.doi.org/10.1103/PhysRevLett.77.3865.

[28] M. Methfessel, A.T. Paxton, High-precision sampling for brillouin-zone integration in metals, Phys. Rev. B 40 (1989) 3616–3621, http://dx.doi.org/10.1103/PhysRevB.40.3616.

[29] A. Togo, I. Tanaka, First principles phonon calculations in materials science, Scr. Mater. 108 (2015) 1–5, http://dx.doi.org/10.1016/j.scriptamat.2015.07.021.

[30] Y. Ikeda, A. Carreras, A. Seko, A. Togo, I. Tanaka, Mode decomposition based on crystallographic symmetry in the band-unfolding method, Phys. Rev. B 95 (2) (2017) http://dx.doi.org/10.1103/physrevb.95.024305.

[31] M.P. Allen, D.J. Tildesley, Computer Simulation of Liquids, Oxford University Press, New York, 2017.

[32] A. Zunger, S.-H. Wei, L.G. Ferreira, J.E. Bernard, Special quasirandom structures, Phys. Rev. Lett. 65 (3) (1990) 353–356, http://dx.doi.org/10.1103/physrevlett.65.353.

[33] A. van de Walle, P. Tiwary, M. de Jong, D. Olmsted, M. Asta, A. Dick, D. Shin, Y. Wang, L.-Q. Chen, Z.-K. Liu, Efficient stochastic generation of special quasirandom structures, CALPHAD 42 (2013) 13–18, http://dx.doi.org/10.1016/j.calphad.2013.06.006.

[34] W. Burgers, On the process of transition of the cubic-body-centered modification into the hexagonal-close-packed modification of zirconium, Physica 1 (7–12) (1934) 561–586, http://dx.doi.org/10.1016/s0031-8914(34)80244-3.

[35] B. Feng, M. Widom, Band structure theory of the bcc to hcp Burgers distortion, Phys. Rev. B 98 (17) (2018) http://dx.doi.org/10.1103/physrevb.98.174108.

[36] K. Persson, M. Ekman, V. Ozolins, Phonon instabilities in bcc Sc, Ti, La, and Hf, Phys. Rev. B 61 (17) (2000) 11221–11224, http://dx.doi.org/10.1103/physrevb.61.11221.

[37] D. de Fontaine, Mechanical instabilities in the b.c.c. lattice and the beta to omega phase transformation, Acta Metall. 18 (2) (1970) 275–279, http://dx.doi.org/10.1016/0001-6160(70)90035-0.

[38] J.M. Sanchez, D. de Fontaine, The omega phase transformation, J. Phys. Colloq. 38 (C7) (1977) 444–452, http://dx.doi.org/10.1051/jphyscol:1977788.

[39] F. Birch, Finite elastic strain of cubic crystals, Phys. Rev. 71 (11) (1947) 809–824, http://dx.doi.org/10.1103/physrev.71.809.

[40] F. Murnaghan, Finite deformation of an elastic solid, Wiley, New York, 1951.

[41] M. Born, Thermodynamics of crystals and melting, J. Chem. Phys. 7 (8) (1939) 591–603, http://dx.doi.org/10.1063/1.1750497.

[42] G. Grimvall, B. Magyari-Kope, V. Ozolins, K.A. Persson, Lattice instabilities in metallic elements, Rev. Modern Phys. 84 (2) (2012) 945–986, http://dx.doi.org/10.1103/revmodphys.84.945.

[43] L. Dezerald, L. Ventelon, E. Clouet, C. Denoual, D. Rodney, F. Willaime, Ab initio modeling of the two-dimensional energy landscape of screw dislocations in bcc transition metals, Phys. Rev. B 89 (2) (2014) http://dx.doi.org/10.1103/physrevb.89.024104.

[44] L. Louail, D. Maouche, A. Roumili, F.A. Sahraoui, Calculation of elastic constants of 4d transition metals, Mater. Lett. 58 (24) (2004) 2975–2978, http://dx.doi.org/10.1016/j.matlet.2004.04.033.

[45] L. Koci, Y. Ma, A.R. Oganov, P. Souvatzis, R. Ahuja, Elasticity of the superconducting metals V, Nb, Ta, Mo, and W at high pressure, Phys. Rev. B 77 (21) (2008) http://dx.doi.org/10.1103/physrevb.77.214101.

[46] J. Li, Y. Wu, Z. Bai, W. Yu, S. Shen, Nanostructure-property relation of $\sum 5$ grain boundary in HfNbZrTi high-entropy alloy under shear, J. Mater. Sci. (2023) http://dx.doi.org/10.1007/s10853-023-08443-1.

[47] Y.X. Ye, B.L. Musico, Z.Z. Lu, L.B. Xu, Z.F. Lei, V. Keppens, H.X. Xu, T.G. Nieh, Evaluating elastic properties of a body-centered cubic NbHfZrTi high-entropy alloy – A direct comparison between experiments and ab initio calculations, Intermetallics 109 (2019) 167–173, http://dx.doi.org/10.1016/j.intermet.2019.04.003.

[48] E.C. Bain, The nature of martensite, Trans. Am. Inst. Min. Metall. Eng. 504 (1924) 70.

[49] K. Masuda-Jindo, S.R. Nishitani, V.V. Hung, Hcp-bcc structural phase transformation of titanium: Analytic model calculations, Phys. Rev. B 70 (18) (2004) http://dx.doi.org/10.1103/physrevb.70.184122.

[50] A.R. Natarajan, P. Dolin, A.V. der Ven, Crystallography, thermodynamics and phase transitions in refractory binary alloys, Acta Mater. 200 (2020) 171–186, http://dx.doi.org/10.1016/j.actamat.2020.08.034.

[51] Y. Lu, P. Zhang, Elasticity behavior, phonon spectra, and the pressure-temperature phase diagram of HfTi alloy: A density-functional theory study, Comput. Mater. Sci. 82 (2014) 5–11, http://dx.doi.org/10.1016/j.commatsci.2013.06.018.

[52] C.-B. Zhang, W.-D. Li, P. Zhang, B.-T. Wang, Phase transition, elasticity, phonon spectra, and superconductive properties of equiatomic TiZr, TiHf, and ZrHf alloys at high pressure: Ab initio calculations, Comput. Mater. Sci. 178 (2020) 109637, http://dx.doi.org/10.1016/j.commatsci.2020.109637.

[53] H. Ledbetter, Elastic properties of zinc: A compilation and a review, J. Phys. Chem. Ref. Data 6 (4) (1977) 1181–1203, http://dx.doi.org/10.1063/1.555564.

[54] N.W. Ashcroft, N.D. Mermin, Solid State Physics, Saunders College, Philadelphia, 1976.

[55] P. Souvatzis, O. Eriksson, M.I. Katsnelson, S.P. Rudin, Entropy driven stabilization of energetically unstable crystal structures explained from first principles theory, Phys. Rev. Lett. 100 (9) (2008) http://dx.doi.org/10.1103/physrevlett.100.095901.

[56] P. Klemens, The scattering of low-frequency lattice waves by static imperfections, Proc. Phys. Soc. A 68 (12) (1955) 1113–1128, http://dx.doi.org/10.1088/0370-1298/68/12/303.

[57] K. Einarsdotter, B. Sadigh, G. Grimvall, V. Ozolins, Phonon instabilities in fcc and bcc tungsten, Phys. Rev. Lett. 79 (11) (1997) 2073–2076, http://dx.doi.org/10.1103/physrevlett.79.2073.

[58] M.J. Lai, C.C. Tasan, J. Zhang, B. Grabowski, L.F. Huang, D. Raabe, Origin of shear induced β to ω transition in Ti-Nb-based alloys, Acta Mater. 92 (2015) 55–63, http://dx.doi.org/10.1016/j.actamat.2015.03.040.

[59] M. Li, X. Min, Origin of ω-phase formation in metastable β-type Ti-Mo alloys: cluster structure and stacking fault, Sci. Rep. 10 (1) (2020) http://dx.doi.org/10.1038/s41598-020-65254-z.

[60] S. Guo, C. Ng, J. Lu, C.T. Liu, Effect of valence electron concentration on stability of fcc or bcc phase in high entropy alloys, J. Appl. Phys. 109 (10) (2011) 103505, http://dx.doi.org/10.1063/1.3587228.

[61] R. Chen, G. Qin, H. Zheng, L. Wang, Y. Su, Y. Chiu, H. Ding, J. Guo, H. Fu, Composition design of high entropy alloys using the valence electron concentration to balance strength and ductility, Acta Mater. 144 (2018) 129–137, http://dx.doi.org/10.1016/j.actamat.2017.10.058.

[62] W. Fang, R. Chang, P. Ji, X. Zhang, B. Liu, X. Qu, F. Yin, Transformation induced plasticity effects of a non-equal molar Co-Cr-Fe-Ni high entropy alloy system, Metals 8 (5) (2018) 369, http://dx.doi.org/10.3390/met8050369.

[63] R. Drautz, D.G. Pettifor, Valence-dependent analytic bond-order potential for transition metals, Phys. Rev. B 74 (17) (2006) http://dx.doi.org/10.1103/physrevb.74.174117.

[64] Y. Tong, S. Zhao, H. Bei, T. Egami, Y. Zhang, F. Zhang, Severe local lattice distortion in Zr- and/or Hf-containing refractory multi-principal element alloys, Acta Mater. 183 (2020) 172–181, http://dx.doi.org/10.1016/j.actamat.2019.11.026.

[65] S. Ishibashi, Y. Ikeda, F. Kormann, B. Grabowski, J. Neugebauer, Correlation analysis of strongly fluctuating atomic volumes, charges, and stresses in body-centered cubic refractory high-entropy alloys, Phys. Rev. Mater. 4 (2) (2020) http://dx.doi.org/10.1103/physrevmaterials.4.023608.

[66] F. Maresca, W.A. Curtin, Theory of screw dislocation strengthening in random BCC alloys from dilute to "High-Entropy" alloys, Acta Mater. 182 (2020) 144–162, http://dx.doi.org/10.1016/j.actamat.2019.10.007.

[67] S. Yin, Y. Zuo, A. Abu-Odeh, H. Zheng, X.-G. Li, J. Ding, S.P. Ong, M. Asta, R.O. Ritchie, Atomistic simulations of dislocation mobility in refractory high-entropy alloys and the effect of chemical short-range order, Nature Commun. 12 (1) (2021) http://dx.doi.org/10.1038/s41467-021-25134-0.

[68] S.I. Rao, B. Akdim, E. Antillon, C. Woodward, T.A. Parthasarathy, O.N. Senkov, Modeling solution hardening in BCC refractory complex concentrated alloys: NbTiZr, $Nb_{1.5}TiZr_{0.5}$ and $Nb_{0.5}TiZr_{1.5}$, Acta Mater. 168 (2019) 222–236, http://dx.doi.org/10.1016/j.actamat.2019.02.013.

[69] B. Chen, S. Li, J. Ding, X. Ding, J. Sun, E. Ma, Correlating dislocation mobility with local lattice distortion in refractory multi-principal element alloys, Scr. Mater. 222 (2023) 115048, http://dx.doi.org/10.1016/j.scriptamat.2022.115048.

[70] P. Singh, B. Vela, G. Ouyang, N. Argibay, J. Cui, R. Arroyave, D.D. Johnson, A ductility metric for refractory-based multi-principal-element alloys, Acta Mater. 257 (2023) 119104, http://dx.doi.org/10.1016/j.actamat.2023.119104.

[71] E. Mak, B. Yin, W.A. Curtin, A ductility criterion for bcc high entropy alloys, J. Mech. Phys. Solids 152 (2021) 104389, http://dx.doi.org/10.1016/j.jmps.2021.104389.

[72] C. Tandoc, Y.-J. Hu, L. Qi, P.K. Liaw, Mining of lattice distortion, strength, and intrinsic ductility of refractory high entropy alloys, npj Comput. Mater. 9 (1) (2023) http://dx.doi.org/10.1038/s41524-023-00993-x.

[73] F. Maresca, W.A. Curtin, Mechanistic origin of high strength in refractory BCC high entropy alloys up to 1900K, Acta Mater. 182 (2020) 235–249, http://dx.doi.org/10.1016/j.actamat.2019.10.015.

[74] C. Baruffi, F. Maresca, W.A. Curtin, Screw vs. edge dislocation strengthening in body-centered-cubic high entropy alloys and implications for guided alloy design, MRS Commun. 12 (6) (2022) 1111–1118, http://dx.doi.org/10.1557/s43579-022-00278-2.

[75] L. Vegard, Die Konstitution der Mischkristalle und die Raumfullung der Atome, Z. Phys. 5 (1) (1921) 17–26, http://dx.doi.org/10.1007/bf01349680.

[76] A.R. Denton, N.W. Ashcroft, Vegard's law, Phys. Rev. A 43 (6) (1991) 3161–3164, http://dx.doi.org/10.1103/physreva.43.3161.

[77] G. Henkelman, A. Arnaldsson, H. Jonsson, A fast and robust algorithm for Bader decomposition of charge density, Comput. Mater. Sci. 36 (3) (2006) 354–360, http://dx.doi.org/10.1016/j.commatsci.2005.04.010.

[78] D. Korbmacher, A. Glensk, A.I. Duff, M.W. Finnis, B. Grabowski, J. Neugebauer, Ab initio based method to study structural phase transitions in dynamically unstable crystals, with new insights on the β to ω transformation in titanium, Phys. Rev. B 100 (10) (2019) http://dx.doi.org/10.1103/physrevb.100.104110.

[79] A. Jackson, On the relationship between omega phase and twinning in bcc structures, Scr. Metall. 22 (3) (1988) 313–316, http://dx.doi.org/10.1016/s0036-9748(88)80196-0.

[80] C.R. Krenn, D. Roundy, J.W. Morris, M.L. Cohen, Ideal strengths of bcc metals, Mater. Sci. Eng. A 319–321 (2001) 111–114, http://dx.doi.org/10.1016/s0921-5093(01)00998-4.